Energy Storage Materials 84 (2026) 104779

Contents lists available at ScienceDirect

Energy Storage Materials

journal homepage: www.elsevier.com/locate/ensm

Ten times of $LiNO_3$ solubility increase in co-solvents free ester-based carbonate electrolytes enables 450 Wh/kg lithium metal batteries

Zhuijun Xu [a,1], Meilan Peng [b,1], Guangjiu Pan [a], Tianle Zheng [a], Yiyao Xiao [b], Weiping Xie [b], Yinghui Li [b,c], Jie Gao [b], Shanshan Yin [d,e], Qing Ji [f], Baohu Wu [g], Yi Miao [h], Siqi Shi [c], Ya-Jun Cheng [b,i,*], Yonggao Xia [b,j,*], Peter Müller-Buschbaum [a,*]

[a] Department of Physics, Chair for Functional Materials, TUM School of Natural Sciences, Technical University of Munich, James-Franck-Str. 1, Garching, 85748, Germany
[b] Ningbo Institute of Materials Technology & Engineering, Chinese Academy of Sciences, 1219 Zhongguan West Rd, Ningbo, 315201, Zhejiang Province, PR China
[c] School of Materials Science and Engineering, Shanghai University, Shanghai, 200444, PR China
[d] The School of Mathematics and Physics, Jiangsu University of Technology, Changzhou, Jiangsu, 213001, PR China
[e] The Jiangsu Key Laboratory of Clean Energy Storage and Conversion, Jiangsu University of Technology, Changzhou, Jiangsu, 213001, PR China
[f] Vehicle Energy and Safety Laboratory, Department of Mechanical Engineering, Ningbo University of Technology, Ningbo 315336, PR China
[g] Jülich Centre for Neutron Science (JCNS) at Heinz Maier-Leibnitz Zentrum (MLZ) Forschungszentrum Jülich, Garching, Germany
[h] Hangzhou Haber Energy Co., Ltd., Hangzhou, Zhejiang, 310000, PR China
[i] College of Renewable Energy, Hohai University, 1915 Hohai Ave, Jintan District, Changzhou, Jiangsu, 213200, PR China
[j] Center of Materials Science and Optoelectronics Engineering, University of Chinese Academy of Sciences, Shijingshan District, Beijing 100049, PR China

ARTICLE INFO

Keywords:
Enthalpy/entropy
Lithium nitrate
Lithium metal batteries
High energy density
Molecular dynamics (MD) simulation

ABSTRACT

$LiNO_3$ is a promising additive for high-energy-density lithium metal batteries (LMBs) *via* regulating the solid electrolyte interphase (SEI) layer. However, the extremely low solubility of $LiNO_3$ in carbonate ester-based electrolytes limits applications. In this study, a two-step physical method successfully dissolves 0.1 M $LiNO_3$ into carbonate ester-based electrolytes without co-solvents (~10 × higher solubility than conventional systems), where EC disrupts Li^+–NO_3^- interactions and the subsequent mixing with a preformed LiFSI/$LiPF_6$–DMC/FEC electrolyte releases part of the coordinated species, increasing entropy, while the remaining solvents/anions stabilize Li^+ - making the process both enthalpically and entropically favorable. This facile, scalable, cost-effective way is confirmed by theoretical simulation and experimental investigations. With the synergistic effect of 4-fluoro-1,3-dioxolan-2-one (FEC), the NO_3^- anions preferentially enter the Li^+ solvation layer. Therefore, the enhanced SEI layer with LiF, Li_xC, and Li_2O homogenizes lithium deposition. The robust cathode–electrolyte interphase (CEI) composed of NSO_xF_y and LiF supports high-voltage Ni-rich cathodes. Notably, Li|| $LiNi_{0.83}Mn_{0.06}Co_{0.11}O_2$ cells retain 82.5 % capacity after 300 cycles at 1 C (1 C = 200 mA g^{-1}) with a 4.3 V cut-off voltage and an 85.5 % capacity after 100 cycles at 1 C with a 4.5 V cut-off voltage. Importantly, a pouch cell with 450 Wh kg^{-1} energy density further demonstrates the practical potential in industry. Additionally, this strategy also demonstrates the potential application of $LiNO_3$ in some carbonated ester-based electrolytes for other alkali metal batteries.

1. Introduction

Lithium-ion batteries (LIBs), a crucial component in the transition to sustainable energy solutions, are widely used in portable electronics, renewable energy storage systems, and electric vehicles (EVs). However, the limited energy density of LIBs (~ 300 Wh kg^{-1}) restricts their applications, especially for use in long-range EVs. Lithium metal has a high specific capacity of 3860 mAh g^{-1} and a low reduction potential (−3.04 V vs. standard hydrogen electrode), promising the realization of high energy density lithium metal batteries (LMBs) [1,2]. Nonetheless, during the cycles, the uncontrolled lithium dendrites due to the unstable solid electrolyte interphase (SEI) layer cause short circuits and safety

* Corresponding authors.
E-mail addresses: chengyj@nimte.ac.cn (Y.-J. Cheng), xiayg@nimte.ac.cn (Y. Xia), muellerb@ph.tum.de (P. Müller-Buschbaum).
[1] These authors contributed equally to this work

https://doi.org/10.1016/j.ensm.2025.104779
Received 10 July 2025; Received in revised form 4 November 2025; Accepted 28 November 2025
Available online 29 November 2025

risks. Additionally, conventional carbonate electrolytes (<4.5 V window) are incompatible with Ni-rich cathodes ($LiNi_xCo_yMn_zO_2$ ($x+y+z=1$, noted as NCM)), leading to unstable cathode-electrolyte interphase (CEI) layers and rapid capacity degradation [3]. Consequently, Li||NCM LMBs have a low energy density, poor lifespans, and potential safety concerns, which have prevented their commercialization so far.

Electrolyte engineering, particularly the incorporation of lithium nitrate ($LiNO_3$) and fluoroethylene carbonate (FEC), plays a critical role in stabilizing Li||NCM LMBs through synergistic regulation of both the SEI and CEI layers. On the anode side, NO_3^- participates in the primary Li^+ solvation sheath and undergoes preferential reduction to generate inorganic species such as Li_2O, Li_3N, and LiN_xO_y, which serve as good Li^+ conductors [4,5]. These components contribute to the formation of a robust SEI layer, enabling homogeneous Li^+ deposition and effectively suppressing dendrite growth [6]. The incorporation of FEC, with its wide electrochemical stability window (>4.5 V), not only further extends the oxidative stability of the electrolyte but also generates LiF upon decomposition, which in turn reinforces both the SEI/CEI layers [7,8]. On the cathode side, NO_3^- facilitates the formation of a passivating electric double layer (EDL), mitigating the decomposition of ether-based electrolytes at high voltages [9]. Moreover, by preferentially entering the Li^+ solvation structure, NO_3^- increases the distances between Li^+ - PF_6^- or Li^+ - FSI^- pairs, thereby suppressing the oxidation of lithium salts at the cathode [10]. In parallel, $LiNO_3$ also scavenges trace water and Lewis acids (e.g., PF_5, Al^{3+}), suppressing HF generation and contributing to more stable CEI/SEI layers [11].

Although $LiNO_3$ can dissolve in ether solvents (e.g., 1,2-dimethoxyethane (DME), diethylene glycol dimethyl ether (DEGDMA)), its low oxidative stability (< 4 V), high viscosity, limited solubility for certain lithium salts, high volatility, and incompatibility with current collectors and NCM cathodes hinder high-energy LMB development [9,12,13]. As for ester-based solvents, in terms of entropy, the strong Li^+ - NO_3^- interaction (donor number (DN) of NO_3^- = 22 kcal mol^{-1}, higher than that of propylene carbonate (PC), being 15 kcal mol^{-1}, dimethyl carbonate (DMC), being 17 kcal mol^{-1}, fluoro-1,3-dioxolan-2-one (FEC)), being 9 kcal mol^{-1}, leads to $LiNO_3$ precipitation and extremely low solubility (<800 ppm, ~0.012 M), insufficient for stabilized SEI and CEI layer formation [1,14–17]. To date, tremendous studies have been devoted to promoting the dissolution of $LiNO_3$ in carbonate ester-based electrolytes, including introducing Lewis acids, using $LiNO_3$ promoters with high polarity and slow release [14,18,19]. Although phosphorus pentachloride (PCl_5), lithium tetrafluoroborate ($LiBF_4$), copper fluoride (CuF_2), aluminum trifluoromethanesulfonate ($Al(OTf)_3$), indium trifluoromethanesulfonate ($In(OTf)_3$), tin trifluoromethanesulfonate ($Sn(OTf)_2$), magnesium bis(trifluoromethanesulfonimide) ($Mg(TFSI)_2$) etc. Lewis acids and high-polarity carriers like isosorbide dinitrate (ISDN), γ-butyrolactone (GBL), tetramethylene sulfone (SL), trimethyl phosphate (TMP), triethyl phosphate (TEP), dimethyl sulfoxide (DMSO), LiTFA can effectively promote the dissolution of $LiNO_3$, [20–25] these approaches suffer from drawbacks such as decomposition, Cu/Al/Sn/In/Mg dendrite growth, electrode corrosion, high viscosity, and poor industrial viability [7,16,26]. Hence, it is urgent to develop a facile, scalable, highly cost-effective, and co-solvent-free ester-based carbonate electrolyte with a high concentration of $LiNO_3$ to meet the requirement of high-energy-density LMBs.

$LiNO_3$ shows a solubility limit of 0.7 M in EC [27]. However, upon introducing DMC, FEC, or other salts (e.g., $LiPF_6$, LiFSI), solvation-structure alterations (entropy changes) drive rapid Li^+–NO_3^- association, causing low solubility [1,16]. Molecular dynamics simulations revealed that the total Gibbs energy of 0.1 M $LiNO_3$ dissolved in an electrolyte with 50 % EC by volume is negative, indicating its thermodynamic stability. Although recent work demonstrated $LiNO_3$ dissolution in $LiPF_6$–EC/DEC/FEC, the mechanism remained unclear [28]. Herein, 0.1 M $LiNO_3$ is successfully dissolved into carbonate ester-based electrolytes without any co-solvents via a two-step physical method, achieving ~10 × higher concentration than conventional systems. Subsequently, the dissolution mechanism from enthalpic, entropic, and binding energy perspectives is clarified. At 55 °C, EC with a high dielectric constant disrupts the strong Li^+–NO_3^- interaction, enabling $LiNO_3$ dissolution. In parallel, LiFSI and $LiPF_6$ dissolve in DMC/FEC at 25 °C. Li^+ ions are initially coordinated with FEC, DMC, FSI^-, and PF_6^-. During the subsequent mixing process, part of the solvents and anions are released from the solvation structure, increasing the reaction entropy, while the remaining FEC, DMC, FSI^-, and PF_6^- in the solvation shell continue to stabilize Li^+ and prevent Li^+–NO_3^- aggregation. Mixing these two pre-electrolytes yields the final electrolyte (0.8 M LiFSI, 0.1 M $LiPF_6$, 0.1 M $LiNO_3$ in EC/DMC or EC/DMC/FEC), referred to as ED-181NFP and EDF-181NFP, respectively. In this method, $LiNO_3$ dissolution is also governed mainly by a strongly negative enthalpy change and a slightly positive entropy change, even with the amount of FEC - typically known to suppress $LiNO_3$ solubility. In contrast, the conventional pathway - directly adding 0.1 M $LiNO_3$ to $LiPF_6$/LiFSI-EC/DMC/FEC electrolytes, is thermodynamically unfavorable. From an enthalpic perspective, pre-coordinated EC reduces the availability of Li^+ for solid $LiNO_3$, while free DMC and FEC lower the dielectric constant, thereby suppressing further $LiNO_3$ solvation. From an entropic perspective, if $LiNO_3$ dissolves, more ester solvents become coordinated, making the process entropically unfavorable [29]. As for EDF-181NFP, the synergistic effect of FEC allows NO_3^- to preferentially enter the Li^+ solvation layer, accompanied by more CIP/AGG solvation structures. A passivating electric double layer (EDL) is formed, which can withstand a higher oxidation potential (~4.7 V) [8]. X-ray photoelectron spectroscopy (XPS) analysis reveals that the enhanced SEI layer is rich in Li_2O, LiF, and Li_xC, promoting the uniformity of lithium deposition, while a robust and thin CEI layer containing NSO_xF_y and LiF optimizes the Li^+ insertion/extraction behavior. Together, the SEI/CEI layers effectively minimize the consumption of lithium salts and solvents, reduce the formation of by-products (Li_2S), and slow down the degradation of SEI/CEI layers. Finally, $LiNO_3$ absorbs trace water to inhibit the formation of corrosive HF and scavenges Lewis acids (e.g., PF_5, Al^{3+}), thereby stabilizing the SEI/CEI layers and FEC, which prolongs the electrolyte lifespan and enhances the cycle life of LMBs. This work presents a simple, scalable, and cost-effective strategy for developing carbonate ester-based electrolytes with $LiNO_3$, providing an in-depth understanding of the mechanism by which the synergistic effect of FEC and LiNO3 stabilizes the SEI/CEI layers.

2. Results and discussion

a) Dissolution ability of $LiNO_3$

In Fig. 1a, two types of clear, transparent ED-181NFP and EDF-181NFP electrolytes are prepared by mixing 0.5 ml of Formulation 1 (0.2 mmol $LiNO_3$ in 1 ml EC at 55 °C) with 0.5 ml of Formulation 2 (3.2 mmol LiFSI and 0.4 mmol $LiPF_6$ in 2 ml DMC), and by mixing 0.5 ml of Formulation 1 with 0.5 ml of Formulation 3 (3.2 mmol LiFSI and 0.4 mmol $LiPF_6$ in 2 ml of a DMC/FEC mixture with a 4:1 vol ratio at 25 °C), respectively. As shown in Fig. 1b, Raman measurements reveal a distinct vibrational peak of N = O at 1045 cm^{-1}, characteristic of NO_3^-, indicating that $LiNO_3$ is successfully dissolved in the ED-181NFP and EDF-181NFP electrolytes [30]. However, two failed electrolytes, named Failed-ED-181NFP and Failed-EDF-181NFP, were obtained by adding 0.1 mmol $LiNO_3$ to 1 ml of ED-81FP (0.8 mmol LiFSI and 0.1 mmol $LiPF_6$ in 1 ml of an EC/DMC mixture with a 5:5 vol ratio at 25 °C) and 1 ml of EDF-81FP (0.8 mmol LiFSI and 0.1 mmol $LiPF_6$ in 1 ml of an EC/DMC mixture with a 5:5 vol ratio at 25 °C), respectively. Thus, with this approach, the molar concentration of dissolved $LiNO_3$ (0.1 M) is approximately ten times higher than that of the current ester-based carbonate electrolytes without co-solvents, which reaches the same level as in the ester-based carbonate with co-solvents (Table S2) [7,8,25,31,32].

Molecular dynamics (MD) simulations are carried out to understand the mechanism for the significant solubility differences of lithium nitrate

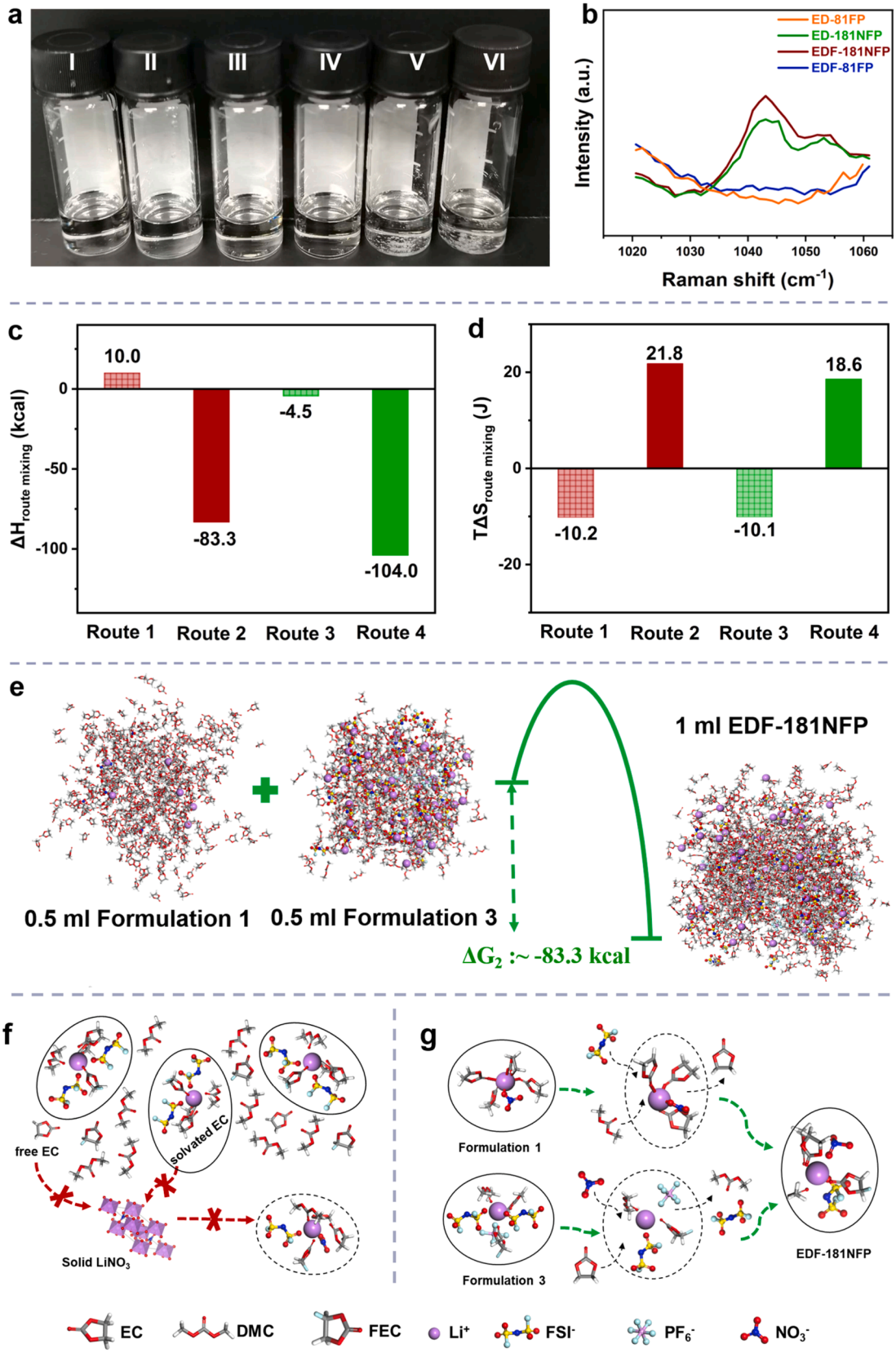

Fig. 1. a) Digital photos of different electrolytes including ED-81FP (**I**), ED-181NFP (**II**), EDF-181NFP (**III**), EDF-81FP (**IV**), Failed-ED-181NFP (**V**), Failed-EDF-181NFP (**VI**); b) Raman spectra of four electrolytes consisting of ED-81FP, ED-181NFP, EDF-181NFP, and EDF-81FP; c,d) Mixing entropy and TΔS under different routes, with temperatures of 328 K and 298 K for the different products, respectively; e) Schematic diagram of Route 2; f, g) Schematic illustration of the processes of Route 1 and Route 2 from the solvation structure.

in co-solvent-free carbonate-based electrolytes. Table S3 shows the enthalpies of various species in MD simulations. Subsequently, the free solvents, free anions, and solvated structures among different species are counted, as shown in Tables S4–S10. Considering the solvation effects, their mixing entropy values are calculated, and the results are displayed in Table S11 by applying the following formula:

$$\Delta S_{mix} = -nR\Sigma x_i \ln x_i \quad (1)$$

where R is the gas constant, n is the total number of moles, and x_i is the mole fraction of component i [29].

We note that the enthalpy of EDF-181NFP is negative and its mixing entropy is positive, indicating that 0.1 M $LiNO_3$ can thermodynamically exist in carbonate ester-based electrolytes. This raises the question of why the solubility of lithium nitrate in carbonate electrolytes is so low experimentally. As displayed in Figure S1 and Fig. 1c-d, in Route 1 (This method is similar to previously reported dissolution approaches when 0.1 M $LiNO_3$ is directly added to 1 M $LiPF_6$- 0.1 M LiFSI in EC/DMC (1:1 by weight) containing 5 % FEC, $LiNO_3$ remains insoluble [29]), the enthalpies of 1.0 mL EDF-181NFP (298 K), 1.0 mL EDF-81FP (298 K), and 0.1 mmol $LiNO_3$ crystal are −35.7 kcal, −41.5 kcal, and −4.2 kcal, respectively (Table S3). Accordingly, $\Delta H_{Route\ mixing}$ for the interaction of 0.1 M $LiNO_3$ crystals with EDF-81FP is approximately 10 kcal (Fig. 1c), indicating that the process is enthalpically unfavorable for dissolution. This is because, on the one hand, EDF-81FP's solvation structure is $Li^+O_{EC}(2.51)O_{DMC}(1.01)O_{FEC}(0.46)O_{FSI}^-(1.56)\ F^-_{PF6}(0.10)\ F^-_{FSI}(0.01)$ (Figure S6c-d), meaning that 30 % (2.51 × 54/460) of EC molecules are already coordinated to Li^+ ions, so fewer free EC molecules are available to coordinate with the Li^+ in solid $LiNO_3$. On the other hand, the free EC mixes with the uncoordinated DMC and FEC, which significantly reduces the electrolyte's dielectric constant, thereby suppressing the further dissolution of $LiNO_3$ (Fig. 1f). From the entropy perspective, compared with EDF-81FP, if $LiNO_3$ were to dissolve, the higher Li^+ concentration in EDF-181NFP leads to more ester solvents being coordinated (as shown in Table S9, EDF-181NFP contains fewer free solvent molecules than EDF-81FP (Table S10)), thereby reducing entropy

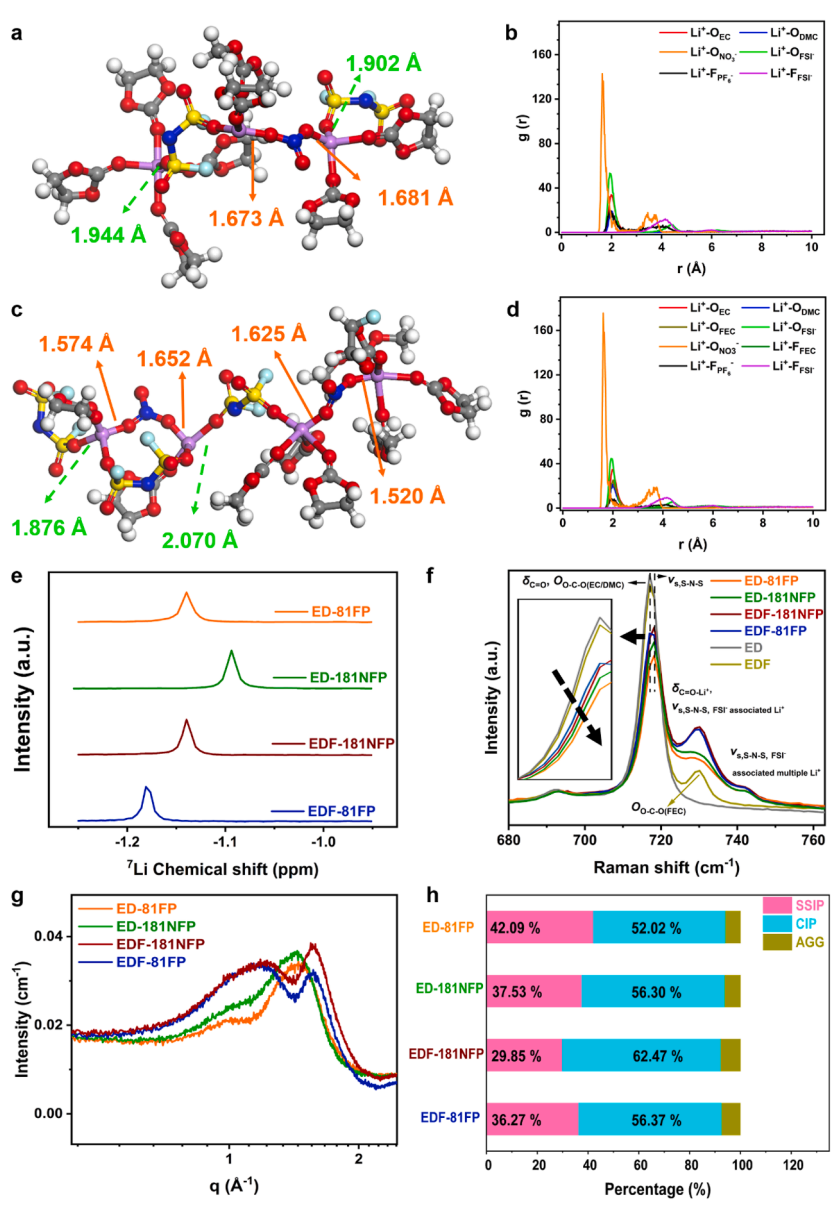

Fig. 2. Clusters in a) ED-181NFP and c) EDF-181NFP. Radial distribution function of Li^+ and anion/solvents in b) ED-181NFP and d) EDF-181NFP at 298 K. e) ^7Li NMR data of four electrolytes; f) Raman and g) SAXS/WAXS spectra of various electrolytes and h) representative Li^+ cation solvate species (SSIP, CIP, and AGGs) in these electrolytes.

(−10.2 J) in Route 1 and making the process entropically unfavorable (Fig. 1d). Finally, the Δ G_1 of the route mixing is positive, suggesting that this Route 1 is not feasible (ΔG greater than zero, indicating a non-spontaneous process). This behavior is not only reflected in the Failed-EDF-181NFP electrolyte, which shows a significant amount of undissolved $LiNO_3$ at the bottom, as displayed in Fig. 1a, but also indicates that in the ternary-salt system, the role of entropy in promoting the solubility of lithium nitrate is limited. Conversely, in the other approach (Route 2, Fig. 1e), 0.2 M $LiNO_3$ is first dissolved in EC (Formulation 1), and the corresponding solvation structure is $Li^+O_{EC}(5.0)$ $O_{NO3}^-(0.5)$ as shown in Figure S4. While other salts, such as LiFSI and $LiPF_6$, are dissolved in DMC and FEC solvents (Formulation 3), and the corresponding solvation structure is $Li^+O_{DMC}(2.11)O_{FEC}(0.90)$ $O_{FSI}^-(2.11)F_{PF6}^-(0.29)$, as displayed in Figure S4e-f. Besides, shown in the Figure S5b, the solvation structure of EDF-181NFP is $Li^+O_{EC}(2.70)$ $O_{DMC}(0.98)O_{FEC}(0.40)O_{FSI}^-(1.21)O_{NO3}^-(0.2)F_{PF6}^-(0.06)$. As for the solvation structure, during the mixing process (Fig. 1*g*), in Formulation 1, 6 $Li^+O_{EC}(5.0)O_{NO3}^-(0.5)$ are transformed into $Li^+O_{EC}(2.70)O_{DMC}(0.98)$ $O_{FEC}(0.40)O_{FSI}^-(1.21)O_{NO3}^-(0.2)F_{PF6}^-(0.06)$. For each solvation structure, 2.7 EC molecules remain coordinated. According to Figure S7a, the binding energy between Li^+ and various solvents or anions shows that 2.7 EC molecules provide a total binding energy of −19.31 kcal mol^{-1}, which is much higher than that of 0.2 NO_3^- (−1.69 kcal mol^{-1}). This ensures that Li^+ and NO_3^- do not remain associated, leading to the precipitation of $LiNO_3$. In Formulation 3, 54 $Li^+O_{DMC}(2.11)O_{FEC}(0.90)$ $O_{FSI}^-(2.11)F_{PF6}^-(0.29)$ are converted into $Li^+O_{EC}(2.70)O_{DMC}(0.98)$ $O_{FEC}(0.40)O_{FSI}^-(1.21)O_{NO3}^-(0.2)F_{PF6}^-(0.06)$. In each solvation structure, 0.98 DMC, 0.40 FEC, 1.21 FSI^-, and 0.06 PF_6^- remain coordinated, providing a total binding energy of −8.24 kcal mol^{-1}, which is still much greater than that of 0.2 NO_3^- (−1.69 kcal mol^{-1}). Therefore, Li^+ and NO_3^- do not remain bound, resulting in the precipitation of $LiNO_3$ as well. More importantly, from the standpoint of entropy, the mixing process leads to the release of additional solvent/anions from the solvation structures, which increases the system's entropy and promotes the reaction. Overall, as presented in the Fig. 1c-d, the $\Delta H_{route\ mixing}$ of Route 2 is around −83.3 kcal, with $T\Delta S_{route\ mixing}$ is 20.9 J. Together, these values result in an overall Gibbs free energy change (ΔG_2) of −83.3 kcal for the formation of EDF-181NFP, confirming the thermodynamic feasibility of this route. The stable solvation structure of Li^+ (where Li^+ does not associate with NO_3^- to form a precipitate), along with a decrease in Gibbs free energy during the above mixing process, ensures that $LiNO_3$ can ultimately dissolve successfully in EDF-181NFP. Similarly, ED-181NFP (0.1 M $LiNO_3$, 0.8 M LiFSI, and 0.1 M $LiPF_6$ in an EC/DMC mixture with a 5:5 vol ratio at 25 °C) can also be prepared using the same method, by mixing Formulation 1 and Formulation 2. In contrast, only Failed ED-181NFP with $LiNO_3$ precipitation can be obtained when 0.1 M $LiNO_3$ crystals are added to ED-81FP (0.8 M LiFSI and 0.1 M $LiPF_6$ in an EC/DMC mixture with a 5:5 vol ratio). For a detailed mechanistic discussion, see the Supporting Information, pages S18–S19.

b) Structure of the electrolytes

MD simulations are further applied to reveal the structure of the electrolytes and interpret the roles of FEC and $LiNO_3$. The formed Li clusters in ED-181NFP and EDF-181NFP are shown in Fig. 2a and 2c. In ED-181NFP, the Li^+-O(NO_3^-) distance is in the range of 1.6–1.7 Å, which is significantly shorter than the Li^+-O(FSI^-) distance (1.9–2.0 Å). In EDF-181NFP, when FEC is added to the cluster, the Li^+-O(NO_3^-) distance is further shortened to below 1.6 Å (1.520 Å in Fig. 2c). To enhance the statistical analysis of lithium-ion coordination, the solvation structures and coordination properties of four electrolytes (ED-81FP, ED-181NFP, EDF-181NFP, and EDF-81FP) are further evaluated using radial distribution functions (RDF), as shown in Fig. 2b, 2d, and Figure S6a, S6c. With the addition of $LiNO_3$ (Fig. 2b, 2d), NO_3^- preferentially enters the solvation shell compared to PF_6^- and FSI^-. Remarkably, when FEC is introduced into the solvent, the probability of nitrate ions being closer to lithium ions increases. These results are consistent with the Li clusters displayed in Fig. 2a, 2c.

As displayed in Figures S5-S6. The first solvation shells (2–4 Å) for ED-81FP, ED-181NFP, EDF-181NFP, and EDF-81FP are as follows: (The oxygen in the solvent is carbonyl oxygen, and the number in brackets is the corresponding coordination number)

ED-81FP: $Li^+O_{EC}(3.31)O_{DMC}(1.28)O_{FSI}^-(1.50)F_{PF6}^-(0.10)F_{FSI}^-(0.03)$ ($F_{FSI}^-(0.03)$ can be neglected.);

ED-181NFP: $Li^+O_{EC}(3.04)O_{DMC}(1.15)O_{FSI}^-(1.21)O_{NO3}^-(0.2)F_{PF6}^-(0.13)$ $F_{FSI}^-(0.03)$ ($F_{FSI}^-(0.03)$ can be neglected.);

EDF-181NFP: $Li^+O_{EC}(2.70)O_{DMC}(0.98)O_{FEC}(0.40)O_{FSI}^-(1.21)$ $O_{NO3}^-(0.2)F_{PF6}^-(0.06)$ $F_{FSI}^-(0.01)$, ($F_{FSI}^-(0.01)$ can be neglected.);

EDF-81FP: $Li^+O_{EC}(2.51)O_{DMC}(1.01)O_{FEC}(0.46)O_{FSI}^-(1.56)$ $F_{PF6}^-(0.10)$ $F_{FSI}^-(0.01)$, ($F_{FSI}^-(0.01)$ can be neglected.).

Compared to EC, the fluorine in FEC causes C=O(FEC) to have fewer electrons than C=O(EC), reducing its binding effect with Li^+. Hence, the binding energy between FEC and Li^+ is lowered, indicating that FEC is a poorer solvent for Li^+. This finding is supported by the observation that the probability of FSI^- entering the solvation shell is higher in EDF-81FP than in ED-81FP (1.56 vs. 1.50). Furthermore, as shown in Tables S3, S11, compared to the corresponding FEC-free samples, the samples with added FEC show an increase in enthalpy and also an increase in entropy. However, the increase in entropy is significantly smaller than the change in enthalpy, which leads to an increase in Gibbs free energy. A higher Gibbs free energy indicates a more unstable system, further confirming that FEC is a poorer solvent compared with EC [27].

Replacing a part of EC with FEC in EDF-181NFP reduces the binding force of solvent molecules to Li^+, thereby strengthening the interaction between Li^+ and NO_3^-. Besides, in the solvation structure of EDF-181NFP, FEC provides a sufficient fluorine source, while $LiNO_3$ contributes inorganic nitrogen and oxygen sources. Decomposition of this solvation structure on lithium metal anodes or cathodes will produce a SEI/CEI layer rich in inorganic components (e.g., LiF, Li_3N, and Li_2O), stabilizing the electrodes/electrolytes interface.

Fig. 2e shows the ^{7}Li NMR results that validate the solvation structures of the electrolytes. In EDF-81FP, on the one hand, FEC reduces its binding effect with Li^+; on the other hand, according to the decrease in the number of EC molecules in the solvation structure and the increase in free EC molecules (around 715 cm^{-1}) observed in the Raman spectra (Fig. 2f (inset)), more EC molecules are excluded from the solvation structure. Thus, the shielding effect is reduced, leading to a downfield shift of the ^{7}Li signal in the spectrum [15]. Conversely, in ED-181NFP, NO_3^- binds strongly to Li^+, causing a high-field shift. Regarding the EDF-181NFP, when FEC partially replaces EC (weaker Li^+ coordination), and due to the presence of NO_3^- (stronger Li^+ coordination), the chemical shift is intermediate, which is similar to that of ED-81FP. More importantly, the NMR results also confirm that 0.1 M $LiNO_3$ can be dissolved in pure ester-based carbonate solvents.

Small- and wide-angle X-ray scattering (SAXS/WAXS) unveils the solvation structures in different electrolytes. In Fig. 2*g*, the SAXS-WAXS profiles show a peak at the scattering vector q position of 1 $Å^{-1}$, which corresponds to the presence of contact ion pairs (CIPs) and aggregates (AGGs) in the electrolyte. Upon the addition of $LiNO_3$ or FEC, this peak shifts toward higher q values and its intensity increases, indicating that both FEC and $LiNO_3$ promote the formation of CIPs and AGGs. Among all samples, the EDF-181NFP shows the highest content of CIP/AGG structures. In this case, the effect of FEC is larger than that of $LiNO_3$ [33]. In addition, a prominent peak around 1.47–1.60 $Å^{-1}$ corresponds to the distance between neighboring atoms of the same anion or adjacent anions [34]. Here, a higher q value means a shorter interatomic distance. When FEC is introduced, as in the EDF-81FP sample, the distance between cations decreases, which is consistent with the solvation structure of EDF-81FP where more FSI^- anions are present. In EDF-181NFP, on the one hand, the presence of fewer solvent molecules in the solvation shell and the weaker solvation ability of FEC allow FSI^- anions to approach each other more easily. On the other hand, the presence of FEC facilitates the aggregation of nitrate anions into the inner solvation shell, leading to a closer packing of nitrate anions.

To better analyze the solvation structure composition of the four samples, Raman spectra are collected in the range of 680–760 cm^{-1}, as shown in Fig. 2f. The band at ~717 cm^{-1} corresponds to the $\delta_{C=O}$ and O_{O-C-O} vibrations of free EC and DMC, while the peak at 718 cm^{-1} arises from the $\nu_{s,\ S\text{-}N\text{-}S}$ mode of free FSI^-, typically assigned to solvent-separated ion pairs (SSIP), i.e., solvation structures without anion participation [35]. The feature at 729 cm^{-1} corresponds to $\delta_{C=O-Li^+}$ (EC or DMC) and $\nu_{s,\ S\text{-}N\text{-}S}$ of FSI^- coordinated with Li^+, which is attributed to contact ion pairs (CIP), i.e., solvation structures involving a single FSI^- anion. The band at 740 cm^{-1} is associated with the $\nu_{s,\ S\text{-}N\text{-}S}$ vibration of FSI^- bound to multiple Li^+ ions, characteristic of aggregates (AGGs) [3,36]. In addition, the O_{O-C-O} vibration of FEC is observed at ~730 cm^{-1} [37]. To quantitatively determine the relative populations of these solvation structures, normalization and deconvolution analyses were performed, as shown in Fig. S9.

As presented in Fig. 2h, when $LiNO_3$ or FEC is added to ED-181NFP or EDF-81FP, the SSIP content decreases and the CIP content increases. The synergy of FEC and $LiNO_3$ in EDF-181NFP further weakens the SSIP structures and enhances the CIP formation, reaching 62.47 %. These results are consistent with the conclusion from SAXS. Compared with free FSI^-, solvated FSI^- is more likely to generate a robust SEI/CEI layer containing more content of inorganic components during cycling, thereby stabilizing the electrodes/electrolytes interface [38].

c) Electrochemical properties and coin-cells performance

The reduction and oxidation behaviors of the five studied electrolytes are examined using cyclic voltammetry (CV). Fig. 3a shows the initial CV curves of ref.ele, ED-81FP, ED-181NFP, EDF-181NFP, and EDF-81FP, recorded over a voltage range of 0.0–2.5 V at a scan rate of 1 mV s^{-1}. Fig. 3b shows density functional theory (DFT) calculations indicating that NO_3^- coordinates with Li^+, resulting in a higher electron affinity of 2.36 eV compared to FSI^-, which exhibits an electron affinity of approximately 0.98 eV. This difference explains why NO_3^- more readily accepts electrons than FSI^-, as evidenced by the NO_3^- reduction peak at 1.22 V in Fig. 3a, whereas the peak at 1.12 V corresponds to the reduction of FSI^- [39]. Additionally, compared to the ref.ele without FEC, the peak at around 1.6 V in EDF-81FP is attributed to the reduction of FEC. When $LiNO_3$ is not added, LiFSI undergoes significant reductive decompositions, as evidenced in the case of ED-81FP. However, the addition of FEC or $LiNO_3$ can reduce the consumption of LiFSI at the expense of a large amount of $LiNO_3$ or FEC, as seen in the cases of ED-181NFP and EDF-81FP. If only FEC is used as an additive, the SEI components primarily originate from FEC, and it can be reasonably inferred that the SEI is mainly composed of organic substances. In the EDF-181NFP, when FEC and $LiNO_3$ work synergistically, all $LiNO_3$, LiFSI, and a tiny amount of FEC are decomposed together. This kind of reduction not only minimizes the consumption of lithium salt but also forms an inorganic SEI layer that suppresses the further decomposition of the solvent.

Tafel curves of Li||Li symmetric cells with various electrolytes are analyzed to determine the exchange current density (i_0) as shown in Fig. 3c. The i_0 values of ref.ele, ED-81FP, ED-181NFP, EDF-181NFP, and EDF-81FP are 1.51 mA cm^{-2}, 2.63 mA cm^{-2}, 2.04 mA cm^{-2}, 8.12 mA cm^{-2} and 4.79 mA cm^{-2}, respectively. The transference numbers of the four studied electrolytes are determined by the classical Bruce-Vincent method [40]. As presented in Fig. 3d, Figure S10, and Table S12, the transference numbers (t_{Li}^+) of ref.ele, ED-81FP, ED-181NFP, EDF-181NFP, and EDF-81FP are 0.44, 0.73, 0.78, 0.75, and 0.69, respectively. Comparing ED-81FP and ED-181NFP, the addition of $LiNO_3$ decreases the exchange current density, likely due to the higher dissociation energy between Li^+ and NO_3^-. It indicates a higher energy barrier for bulk transport and sluggish interfacial oxidation, resulting in continuous decomposition between electrolytes and electrodes [30,41]. Correspondingly, as $LiNO_3$ is added, the lithium-ion transference number (t_{Li}^+) rises, which is attributed to the strong interaction between Li^+ and NO_3^-. A higher transference number helps to reduce the concentration polarization, thereby preventing the formation of lithium dendrites. Conversely, in the case of EDF-81FP, when only FEC is added, its t_{Li}^+ number is decreased, which originates from the higher viscosity of

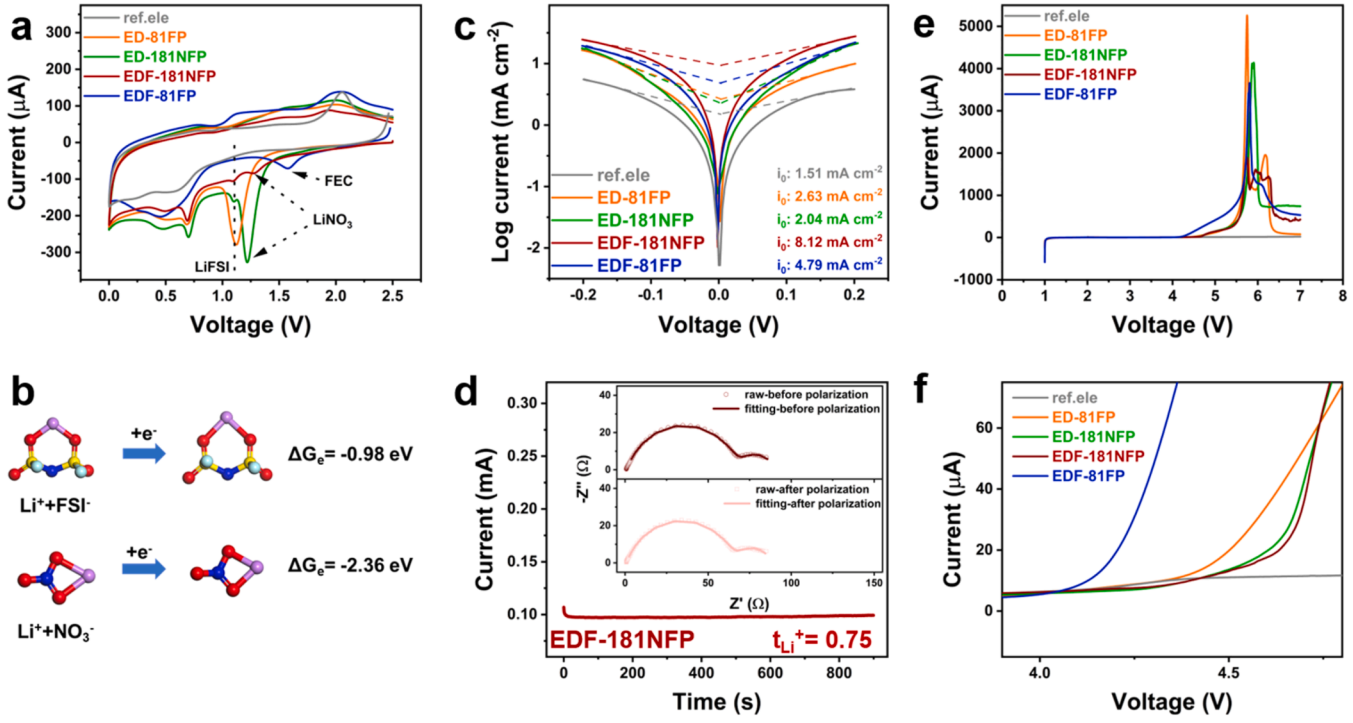

Fig. 3. a) Initial cyclic voltammetry (CV) curves for Li||Cu cells with five different electrolytes. b) Electron affinity of optimized Li^+-anion complexes obtained from DFT calculations. c) Tafel curves of Li||Li symmetric cells with various electrolytes used to determine the exchange current density (i_0). d) Current curves of Li||Li symmetric cells for EDF-181NFP, used to calculate the transference number (inset: corresponding electrochemical impedance spectroscopy (EIS) measurements before and after polarization). e–f) Linear sweep voltammetry (LSV) tests of Li||Al cells with different electrolytes, including a magnified view of selected regions.

FEC [42]. For EDF-181NPF, previous RDF and NMR analyses revealed that FEC participates in the solvation structure. However, FEC is a poor solvent for lithium nitrate, which destabilizes lithium nitrate within the solvation structure and accelerates its decomposition. This finding explains the rapid increase in i_0 observed in EDF-181NFP. Additionally, the increased viscosity caused by FEC slightly hinders ion mobility, leading to a tiny decrease in the transference number of EDF-181NFP to 0.75. In EDF-181NFP, $LiNO_3$ and FEC synergistically regulate the electrolyte transference number and exchange current density, facilitating the uniform and stable growth of lithium.

Additionally, as presented in Figs. 3e-f and S11, for ED-81FP, due to the corrosion of stainless steel and Al foil by LiFSI, the oxidation potential is around 4.3 V, which is consistent with the literature [43,44]. Upon the addition of FEC, however, LiFSI and trace water generate HF, which can attack Al foil or stainless steel to form Al^{3+} and Fe^{3+} [45]. Additionally, $LiPF_6$ and trace water produce HF and PF_5. These Lewis acids (PF_5, Al^{3+}) can further attack the F atoms in FEC, producing more HF and accelerating Al corrosion, as clearly evidenced by the SEM images in Figure S12 [46]. Consequently, the oxidation potential of EDF-81FP decreases to ~4.10 – 4.15 V. In contrast, the introduction of $LiNO_3$ enables the formation of a passivating layer on Al foil or stainless steel surfaces and scavenges trace water, thereby mitigating the corrosion of lithium salts toward the current collector and the battery casing [11]. Importantly, $LiNO_3$ also scavenges Lewis acids (e.g., PF_5 and Al^{3+}), protecting FEC and allowing the electrolyte to operate stably at high voltages [11]. As a result, both ED-181NFP and EDF-181NFP exhibit significantly enhanced oxidation potentials on stainless steel and Al foil, exceeding 4.5 V [9]. Although the oxidation stability of ED-181NFP and EDF-181NFP remains slightly lower than that of the ref.ele, they are nevertheless adequate to sustain the operation of ~4.5 V high-voltage lithium metal batteries, underscoring the practicality and stability of our formulated electrolytes. In particular, when considering factors such as oxidative potential, t_{Li}^{+}, and i_0, EDF-181NFP demonstrates overall superior performance compared to the reference electrolyte, ED-81FP, ED-181NFP, and EDF-81FP.

The EIS spectrum of the Li||Li symmetric cells based on the five electrolytes before cycling is displayed in Fig. 4a, which is the same as the EIS tests for determining the transference number. The first semicircle at high frequency represents the interface impedance of the passivating layer (R_{pl}), and the second semicircle corresponds to the charge transfer impedance (R_{ct}). R_{pl} corresponds to R_0 in Table S12. Among the four samples, Li||Li symmetric cells with EDF-181NFP have the lowest R_{pl} and R_{ct} values, comparable to those of the ref.ele, indicating excellent wettability toward lithium metal. As shown in Fig. 4b, thanks to its superior wettability, high t_{Li}^{+} and i_0, Li||Li symmetric cells with EDF-181NFP display the lowest voltage polarization among all tested electrolytes. Additionally, the cells with EDF-181NFP demonstrate a cycling stability of approximately 380 cycles, whereas the cells with ref.ele, ED-81FP, ED-181NFP, and EDF-81FP short-circuit after 150–250 cycles due to the formation of unstable lithium dendrites. Subsequently, the Li||Cu coin cells are further used to evaluate lithium plating/stripping behaviors within the five electrolytes. As shown in Fig. 4c-d, the initial coulombic efficiency of Li||Cu coin cells with EDF-181NFP is 95.91 %, outperforming ref.ele, ED-81FP, ED-181NFP, and EDF-81FP, which only achieve 83.15 %, 80.51 %, 89.16 %, and 94.06 %, respectively. Moreover, EDF-181NFP exhibits the lowest absolute lithium deposition overpotential among the five electrolytes (Fig. 4e), suggesting that the largest lithium grain size is an important factor for

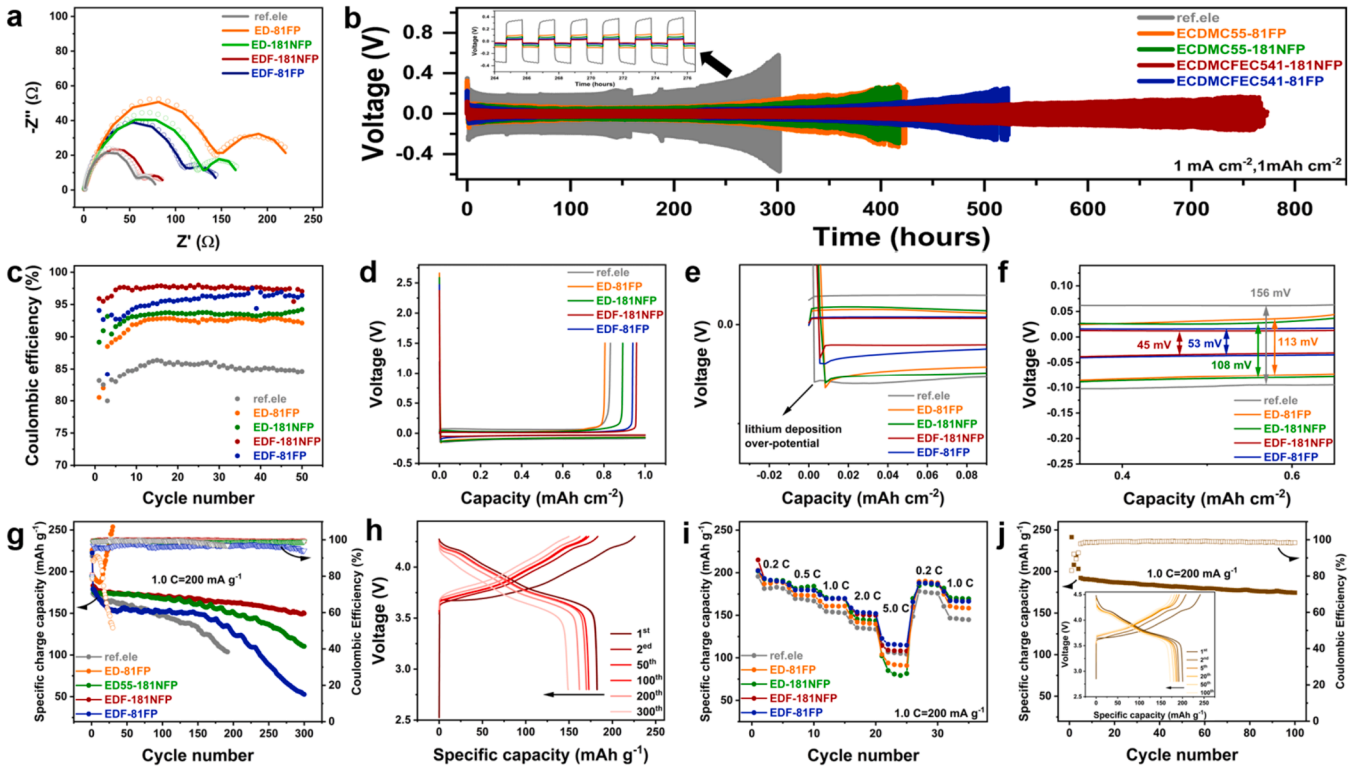

Fig. 4. a) EIS measurements of Li||Li symmetric cells with various electrolytes (ref.ele, ED-81FP, ED-181NFP, EDF-181NFP, EDF-81FP) before galvanostatic cycling. b) Galvanostatic cycling of Li||Li symmetric cells with a capacity of 1 mAh cm^{-2} and a current density of 1 mA cm^{-2} in the five electrolytes: ref.ele, ED-81FP, ED-181NFP, EDF-181NFP, and EDF-81FP, with the inset showing localized charge/discharge curves of five different samples. c) Coulombic efficiencies of Li||Cu cells (capacity of 1 mAh cm^{-2}) during discharge at a current density of 1.0 mA cm^{-2} and charge at 0.5 mA cm^{-2}. d–f) Initial plating/stripping profiles for Li metal on a Cu foil substrate in the five electrolytes, along with corresponding magnified views (e, f). g) Charge capacity and Coulombic efficiencies of Li||Ni83 cells cycled between 2.8 V and 4.3 V at 1.0 C (1.0 C = 200 mAh g^{-1}). h) Charge/discharge curves of Li||Ni83 cells over various cycles using EDF-181NFP. i) Rate performance of Li||Ni83 cells at different current densities with a voltage range of 2.8 V to 4.3 V. j) Charge capacity and Coulombic efficiencies of Li||Ni83 cells cycled in EDF-181NFP with a voltage range of 2.8 V to 4.5 V at 1.0 C (1.0 C = 200 mAh g^{-1}), with the inset showing charge/discharge curves during different cycles.

achieving uniform and stable lithium deposition [47]. Notably, during the charge/discharge process, Li||Cu cells with EDF-181NFP show the smallest voltage polarization, measured as just 45 mV (Fig. 4f), compared to 156, 53, 108, and 113 mV for ref.ele, ED-81FP, ED-181NFP, and EDF-81FP, respectively. This reduced polarization is attributed to a superior wettability, high t_{Li}^{+} and i_0. The morphology of the lithium deposits after the first plating, shown in Figure S13, further supports this finding. In EDF-181NFP, the lithium deposits are the largest and exhibit the lowest porosity, resulting in reduced interfacial resistance and aligning with the observed low overpotential and polarization during cycling. Therefore, after 50 cycles, the Li||Cu cells with EDF-181NFP maintain a high average coulombic efficiency of 97.40 %, surpassing the efficiencies of 85.02 %, 91.78 %, 93.24 %, and 95.33 % for ref.ele, ED-81FP, ED-181NFP, and EDF-81FP, respectively. The superior performance of EDF-181NFP reflects a lower consumption rate of lithium metal and contributes to an extended lifespan for lithium metal batteries.

Fig. 4g-h and Figure S14 present the evaluation of five electrolytes ED-81FP, ED-181NFP, EDF-181NFP, EDF-81FP and ref.ele in Li||Ni83 coin cells. The Ni83 electrode bears a mass loading of 9 mg cm^{-2}, corresponding to a theoretical area capacity of 1.8 mAh cm^{-2}. The thickness and radius of the lithium metal used here are 250 μm, and 16 mm, respectively. The initial specific capacities of the cells with all five electrolytes are approximately 180 mAh g^{-1}. The Li||Ni83 coin cells using the ED-81FP exhibit a rapid overcharging, primarily due to the limited stability of LiFSI at high voltages, as reported in previous studies [48]. This is also evident in Figure S15a, where a large leakage current is observed when the voltage is maintained at 4.3 V in Li||Ni83 cell with ED-81FP [49]. This issue is effectively mitigated by the addition of FEC. As shown in Figure S15a, the initial current for EDF-81FP is relatively high, indicating that CEI formation is consuming a huge lithium source from the cathode or electrolytes. In Fig. 4g, this is reflected by the rapid capacity drop during the first few cycles. Once a stable CEI layer forms, the leakage current decreases to 19 μA (Figure S15b). In subsequent cycles, within the EDF-81FP electrolyte, the Li||Ni83 coin cells achieve 143 cycles before the capacity drops to 80 % of its initial value, followed by rapid capacity degradation. By introducing electrolytes containing $LiNO_3$, such as ED-181NFP and EDF-181NFP, a significantly improved battery performance is achieved. $LiNO_3$ forms a passivating double layer on the cathode particle surfaces, consuming a smaller amount of the lithium source during the initial CEI formation. This stable CEI layer maintains a low leakage current, thereby minimizing solvent and lithium salt consumption and prolonging the electrolyte and cell lifespan.

When both FEC and $LiNO_3$ are present in EDF-181NFP, the Li||Ni83 coin cells retain a capacity of 149 mAh g^{-1} after 300 cycles, with a capacity retention of 82.5 %. Additionally, the average coulombic efficiency over 300 cycles reaches 99.62 %, outperforming the values of 99.01 %, 98.57 % and 96.57 % achieved by ref.ele, ED-181NFP and EDF-81FP, respectively. The coin cells using ED-81FP electrolytes only last 30 cycles, rendering their coulombic efficiency negligible. Compared with $LiNO_3$-containing electrolytes reported in the literature (either ether-based electrolytes or those employing high-polarity carriers to assist $LiNO_3$ dissolution) (Table S13), the Li||Ni83 coin cell also exhibits outstanding performance.

The rate performance of the five electrolytes ref.ele, ED-81FP, ED-181NFP, EDF-181NFP, and EDF-81FP is evaluated, as shown in Fig. 4i. The addition of $LiNO_3$ negatively affects the rate performance in the ED-181NFP, likely due to a thicker passivation electric double layer, which hinders Li^+ migration at high current densities. When FEC is present in EDF-181NFP, it drives NO_3^- more into the inner solvation shell, thereby reducing the thickness of the EDL and alleviating this issue. The formation of a CEI layer containing LiF and LiN_xO_y helps to compensate for the reduced rate performance. As a result, Li||Ni83 coin cells with EDF-181NFP still achieve an acceptable capacity of 109 mAh g^{-1} at a current density of 5.0 C. Remarkably, as shown in Fig. 4j, the Li||Ni83 cell with EDF-181NFP can operate at a cutoff voltage of 4.5 V, maintaining a capacity retention of 85.7 % after 100 cycles, which provides the possibility of higher energy density lithium metal batteries.

d) Interfacial analysis- SEI & CEI Layers

Firstly, the surface morphology of lithium metal in Li||Li symmetric cells after 50 cycles at a capacity of 1 mAh cm^{-2} and a current density of 1 mA cm^{-2} is analyzed using SEM, as shown in Fig. 5a-5d These cells are cycled in the four electrolytes ED-81FP, ED-181NFP, EDF-181NFP, and EDF-81FP. Like the morphology observed in Li||Cu cells after the first charging process, after 50 cycles, the lithium metal in ED-81FP cells exhibits the presence of prominent lithium dendrites and numerous voids on the surface (Fig. 5a). However, with the presence of $LiNO_3$ (ED-181NFP) or FEC (EDF-81FP), as depicted in Figs. 5b and 5d, lithium dendrites are nearly absent, and replaced by a moss-like lithium structure consisting of small particles (0.5–1.0 μm) with fewer voids. Notably, when both FEC and $LiNO_3$ are combined (EDF-181NFP), large, dense lithium blocks form with minimal voids (Fig. 5c), indicating a significantly improved surface morphology.

X-ray photoelectron spectroscopy (XPS) combined with etching technology is used to further reveal the SEI composition of Li||Li symmetric cells and the CEI composition of Ni83||Li cells after 50 cycles for the four electrolytes (ED-81FP, ED-181NFP, EDF-181NFP, and EDF-81FP). No distinct peaks are seen in the P 2p spectrum (see Figure S16), indicating that $LiPF_6$ is not negligibly consumed on the surface of the anodes. Furthermore, the absence of components such as LiP_xF_y and $LiP_xO_yF_z$ in the fluorine spectrum is essential for accurately analyzing fluorine-containing species.

In the O 1 s spectrum as presented in Figs. 5e and S17, the peaks of C=O, SO_x/NSO_xF_y, C-O, and Li_2O are observed at 528.0 eV, 531.4 eV, 532.4 eV, and 534.0 eV, respectively [50,51]. As for the SEI layers, in Fig. 5i, the Li_2O exhibits a gradient distribution with depth across all samples, and in the EDF-181NFP sample, the content reaches its highest level due to the shorter distance between Li-O (NO_3^-) in the lithium-ions clusters under the influence of FEC. It means that FEC promotes the rapid conversion of $LiNO_3$ into Li_2O, and subsequently, the dense Li_2O-containing SEI layer not only facilitates a rapid lithium-ion transport but also slows down the consumption of $LiNO_3$, EC, DMC, FEC, LiFSI, and $LiPF_6$ on both the anode and cathode-

The F 1 s spectrum is displayed in Figs. 5f, S18 and S24. The peaks situated at 685.0 eV, 685.6 eV, 687.6 eV, 688.3 eV originate from LiF, semi ionic C-F, NSO_xF_y, and S-F/covalent C-F, respectively [52,53]. With the addition of $LiNO_3$ in the ED-181NFP sample, as shown in Figures S18b and S19a, the LiF is more likely to be generated in SEI layer. A small amount of C-F comes from the reaction of F separated from LiFSI with solvents such as EC and DMC [54]. Although the addition of FEC provides more fluoride sources in EDF-81FP, the incomplete reduction of FEC also leads to the formation of a significant amount of organic C-F compounds alongside the large production of LiF (Figures S18d and S19). A synergistic effect exists between $LiNO_3$ and FEC in EDF-181NFP, forming a dense Li_2O-containing SEI layer. This layer also protects FEC, minimizing its reduction at the anode with less organic C-F (Figure S19b), which aligns with the results shown in Fig. 3a. Regarding the CEI layers, in the EDF-181NFP sample, the peaks of NSO_xF_y (main components) and LiF with strong intensity are observed in Figs. 5f and 5m Besides, $LiNO_2$ is also detected (see Figure S28) under the dual passivation effect of FEC and $LiNO_3$ on Ni83 cathodes. LiFSI and $LiNO_3$ undergo a partial decomposition, leading to intermediate products, including NSO_xF_y, $LiNO_2$, LiF inorganic components alongside with less organic C-F (see Figure S25), which contributes to a robust CEI formation [55,56].

The less consumption of solvents (EC, DMC, FEC) and lithium salts (LiFSI, $LiPF_6$) on the anodes and cathodes in the samples with the additives is further proven by the S 2p, N 1 s and C 1 s spectra. Regarding the S 2p spectrum (Figs. 5g, S20 and S27), the peaks located at around 170.0 eV, 169.3 eV, 167.3 eV, 163.0 eV and 161.0 eV belong to NSO_xF_y, NSO_x, SO_3^{2-}, polysulfide and Li_2S, respectively [57–59]. Concerning the

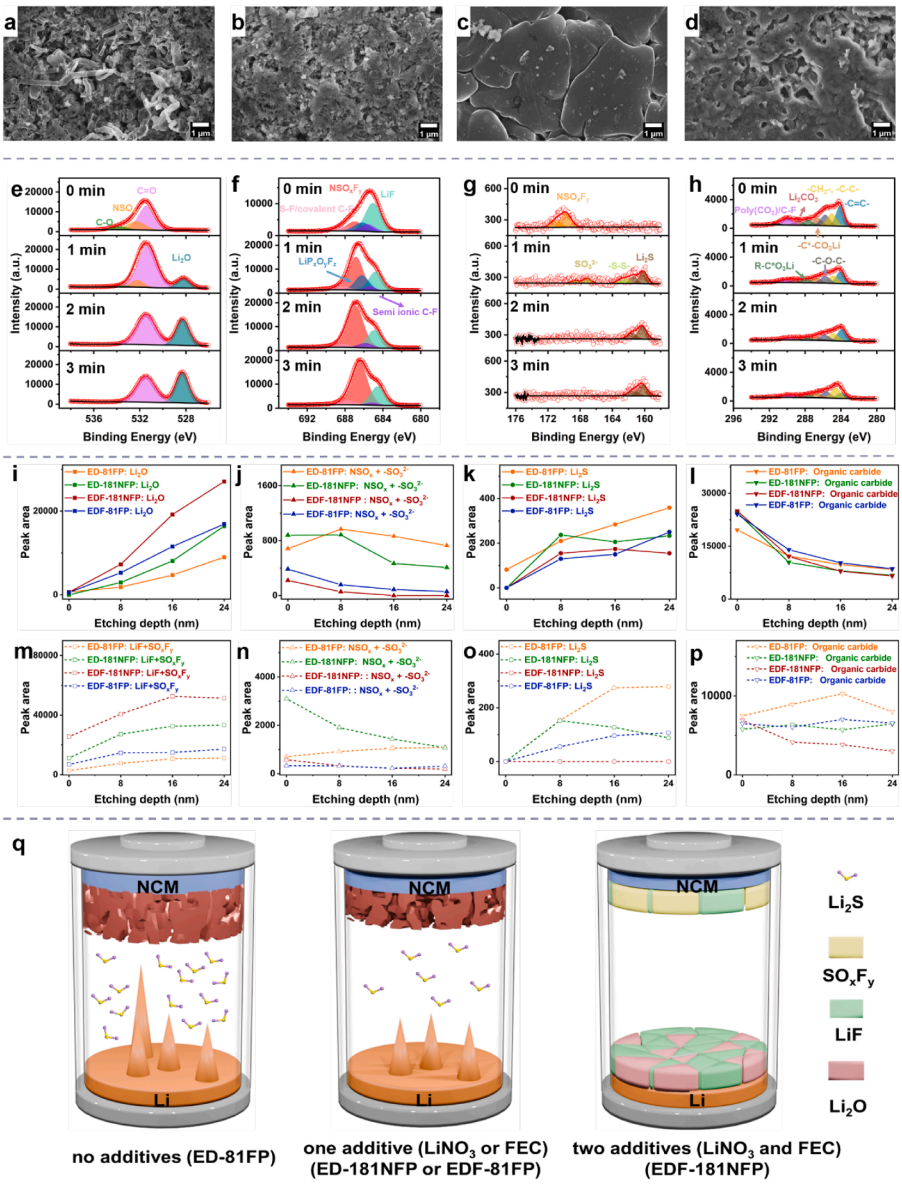

Fig. 5. SEM images of the lithium deposition morphology after 50 cycles in Li||Li symmetric cells with a capacity of 1 mAh cm^{-2} and a current density of 1 mA cm^{-2} in the four electrolytes: a) ED-81FP, b) ED-181NFP, c) EDF-181NFP, and d) EDF-81FP. XPS measurements: (e, g) O 1s, S 2p spectra of SEI layers in Li||Li symmetric cells after 50 cycles with a capacity of 1 mAh cm^{-2} and a current density of 1 mA cm^{-2} using EDF-181NFP; (f, h) F 1s, C 1s, spectra of CEI layers in Ni83||Li cells after 50 cycles with voltage cut-off of 4.3 V and 1 C (1C=200 mA g^{-1}) current density using EDF-181NFP (The etching time is 0, 1, 2, 3 minutes, respectively, and the etching rate is 8 nm/min); (i-l) peak area of the corresponding substances of the SEI layers in different etching depths with different electrolytes; (m-p) peak area of the corresponding substances of the CEI layers in different etching depths with different electrolytes. (The peak area of Li_2S is based on the Li_2S $2p_{3/2}$ peak, while the peak areas of NSO_x/NSO_xF_y and SO_3^{2-} are based on the NSO_x/NSO_xF_y and SO_3^{2-} $2p_{3/2}$ peaks, respectively.) q) Schematic illustration of the SEI and CEI layers in LMBs in the four electrolytes.

N 1 s spectrum, (Figures S21 and S28), the peaks located at 398.7 eV, and 400.3 eV, are corresponding to the Li_3N, $NSO_x/NSO_xF_y/LiN_xO_y$, respectively. Herein, sulfur-containing compounds are solely derived from the decomposition of LiFSI, while nitrogen-containing compounds are partially attributed to LiFSI decomposition. For the electrolytes containing $LiNO_3$, nitrogen-containing compounds also originate from the decomposition of $LiNO_3$. Notably, as depicted in Fig. 5j, when additives (FEC, $LiNO_3$, or FEC & $LiNO_3$) are present, the content of NSO_x and SO_3^{2-} is reduced in the SEI layer (compared to the ED-81FP electrolyte). In the corresponding nitrogen spectrum (Figures S21 and S22), Li_3N is also weakened, while NSO_x increases. This finding suggests that the addition of $LiNO_3$ or FEC mitigates the consumption of LiFSI and inhibits the complete decomposition of LiFSI. Besides, as shown in Figs. 5n, S26, and S27, as for the cathode in ED-181NFP, the surface contents of $LiP_xO_yF_z$, NSO_x, and SO_3^{2-} are relatively high but decrease as the etching depth increases. This finding indicates that once $LiNO_3$ is extensively consumed on the anodes, it can no longer serve as a passivation layer on the cathodes, and LiFSI and $LiPF_6$ will be significantly depleted. Therefore, when $LiNO_3$ is protected by FEC, as in the case of EDF-181NFP, the consumption of lithium salts on both electrodes is significantly reduced, thereby enhancing the battery lifespan. More importantly, the addition of $LiNO_3$ or FEC reduces the content of Li_2S on both SEI and CEI layers (Figs. 5k and 5o). In EDF-181NFP, their contents are minimized. As a result, the shuttling effect of lithium sulfide is significantly suppressed, thereby stabilizing the SEI and CEI layers.

As for the C 1 s spectrum, shown in the Figs. 5h, S23, and S29, the peaks located at 282.6 eV, 284.0 eV, 284.8 eV, 286.0 eV, 286.6 eV, 288.1 eV, 289.5 eV and 290.2 eV, are attributed to the Li_xC, -C=C-,

-CH_2-/-C-C-, -C-O-C-, -C*-CO_2Li, and R-C*O_3Li, Li_2CO_3 and poly(CO_3)/C-F, respectively [51,53,54,59,60]. As for the SEI layers, in ED-181NFP and EDF-81FP electrolytes, as shown in Figure S23, the addition of $LiNO_3$ or FEC leads to an increase in the lithium-philic compound-Li_xC content with etching depth, while FEC has a more pronounced effect [60]. Among the four samples, EDF-181NFP exhibits the highest Li_xC content. With the assistance of $LiNO_3$ in ED-181NFP and EDF-181NFP, as shown in Fig. 5l, the total peak areas of organic carbide including -C=C-, -CH_2-/-C—C-, -C-O—C-, -C*-CO_2Li, and R-C*O_3Li, Li_2CO_3 and poly(CO_3)/C-F is the lower, which indicates that $LiNO_3$ (or dense Li_2O-containing SEI layer formed by $LiNO_3$) helps to mitigate the degradation of organic solvents such as EC, DMC, and FEC. However, FEC has a negative effect, increasing the content of organic carbide due to its tendency to be easily reduced at the anode, which is consistent with the huge amount of organic C-F in the F 1 s spectrum. In the CEI layers, originating from the antioxidative properties of FEC and passivation effect of $LiNO_3$, the total peak areas of organic carbide including -C=C-, -CH_2-/-C-C-, -C-O-C-, -C*-CO_2Li, and R-C*O_3Li, Li_2CO_3 and poly(CO_3)/C-F in the EDF-181NFP is also lowest (Fig. 5p), which reduces interfacial resistance and enhances battery performance.

Originating from less consumption of solvents (EC, DMC, FEC) and lithium salts (LiFSI, $LiPF_6$) on cathodes, the lattice-oxygen peak located at 529.3 eV is detectable at an etching depth of just 8 nm in the EDF-181NFP sample (Figure S30). In contrast, in the other three samples, it only appears at depths of 16 nm or greater. This observation indicates that the CEI layer in EDF-181NFP is the thinnest among the four samples.

Overall, as shown in Fig. 5q, the incorporation of FEC and $LiNO_3$ in the EDF-181NFP promotes the formation of a distinctive SEI and CEI layers. In the SEI layers, FEC promotes the rapid decomposition of $LiNO_3$. Subsequently, the dense Li_2O-containing SEI layer formed by $LiNO_3$ prevents FEC from being extensively reduced. Thus, a robust SEI layer with a gradient distribution of lithium-philic Li_xC, inorganic components Li_2O, as well as a proportion of LiF with fewer organic components, is constructed. Under the dual passivation effect of $LiNO_3$ and FEC on the cathode side, a thin and durable CEI comprising NSO_xF_y (main components), $LiNO_2$, and LiF inorganic components with fewer organic components stabilizes the cathode and the cathode-electrolyte interface. The unique SEI and CEI layers, on the one hand, reduce the interfacial resistance and accelerate the lithium-ion transport. On the other hand, they effectively minimize the consumption of lithium salts and solvents, thereby reducing the formation of by-products (Li_2S), which slows down the degradation rate of SEI/CEI layers.

e) Pouch-cell performance

Finally, as shown in Figs. 6a and 6b, an experimental 6 Ah pouch cell (78.0 mm × 58.0 mm × 4.5 mm) with EDF-181NFP is fabricated and evaluated for its electrochemical performance. A 70 μm Li–Mg alloy was used as the anode and current collector, whose solid-solution structure restricts lithium diffusion, enables uniform deposition, suppresses dendrites and side reactions, and accommodates volume changes without compromising energy density [61,62]. The pouch cell is tested with a voltage range from 2.8 V to 4.35 V and a C-rate of 0.5 C (1.0 C = 6 A) at room temperature. As depicted in Figs. 6c and 6d, At an ultralow N/P ratio (≈1.27), the pouch cell exhibits an energy density of 474 Wh/kg during the first cycle of charging, maintained a gravimetric energy density of around 450 Wh/kg and a volumetric energy density of 710 Wh L^{-1} in the subsequent cycles, and is able to retain 405 Wh/kg after 20 cycles. Although the capacity can be slightly restored after adding another 4 g electrolyte in the subsequent process, the pouch cell fails after 35 cycles. Nonetheless, this method has validated the feasibility of

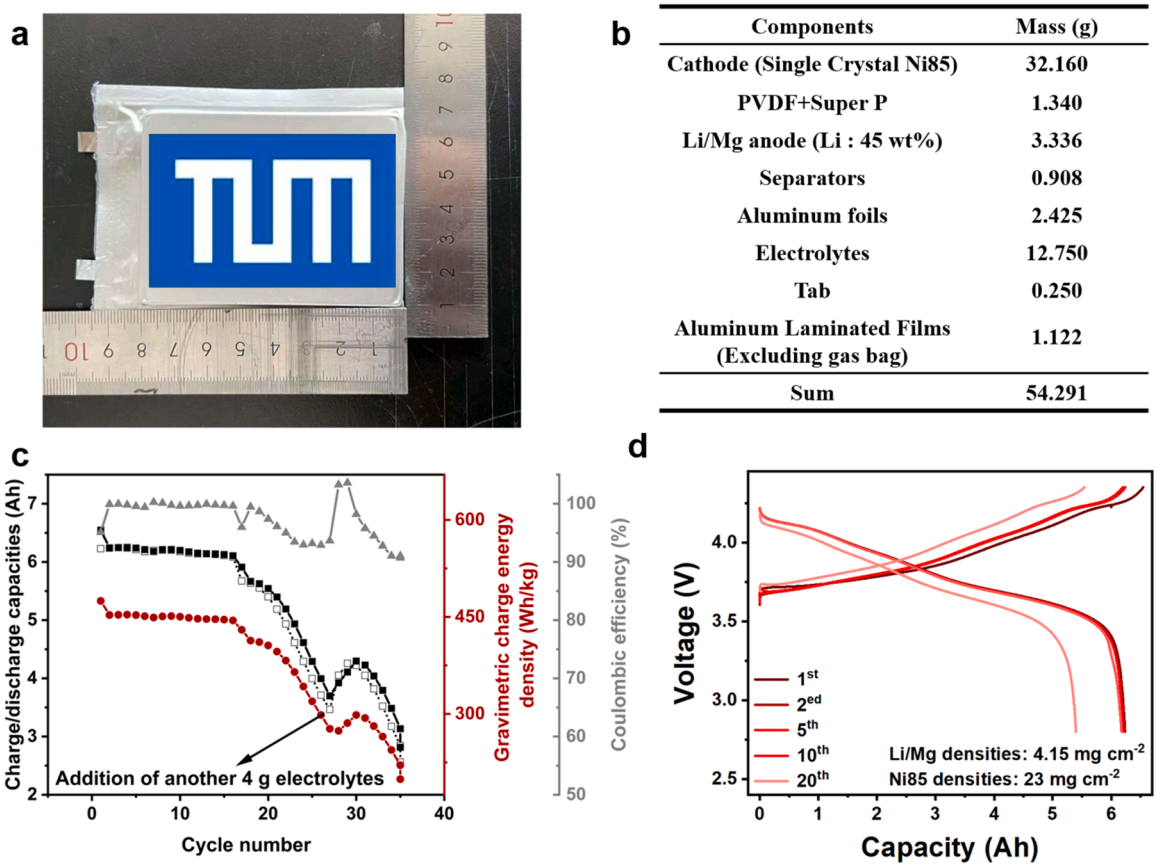

Fig. 6. a) Digital photograph of a 6 Ah pouch cell. b) Composition and corresponding mass of the 6 Ah pouch cell (Electrolytes: EDF-181NFP) and the N/P ratio≈1.27. c) Charge capacity and corresponding energy densities of the pouch cell cycled between 2.8 V and 4.35 V at 0.5 C (1.0 C = 6 A). d) Charge/discharge curves of the pouch cell over various cycles.

using $LiNO_3$ additives in pure ester-based carbonate electrolytes for fabricating high-energy-density lithium metal batteries, with further optimization possible in the future.

3. Conclusion

In summary, we report a simple, scalable, co-solvent–free two-step method that dissolves 0.1 M $LiNO_3$ in carbonate ester electrolytes, achieving ~10 × higher solubility than conventional systems. In the first step, EC at elevated temperatures disrupts Li^+–NO_3^- interactions, forming $Li^+O_{EC}(5.0)O_{NO3^-}(0.5)$. Simultaneously, in the preformed LiFSI/$LiPF_6$–DMC/FEC electrolyte, Li^+ ions are initially coordinated with FEC, DMC, FSI^-, and PF_6^-. During the subsequent mixing process, the solvation structure releases part of the solvents/anions, increasing the reaction entropy, while the remaining FEC, DMC, and FSI^-, PF_6^-in the solvation shell stabilize Li^+ and prevent Li^+–NO_3^- aggregation. The mixing process is both enthalpically and entropically favorable. MD simulations, ^{7}Li NMR, and Raman spectroscopy confirm that NO_3^- enters the Li^+ solvation sheath. Upon the addition of FEC, interactions between NO_3^- and Li^+ are enhanced, leading to an improved CIP/AGG solvation structure, lithium-ion mobility, and exchange current density. This solvation structure also contributes to the stability of $LiNO_3$-containing electrolytes on lithium metal anodes, Al foils, stainless steel 316, and Ni83 cathodes. A unique SEI layer is formed, which has a gradient distribution of lithium-philic Li_xC, inorganic components such as Li_2O, and a proportion of LiF, along with fewer organic components. Furthermore, with the dual passivation effect of $LiNO_3$ and FEC on the cathode side, a thin and robust CEI comprising a substantial number of inorganic components (NSO_xF_y, $LiNO_2$, and LiF) with fewer organic components is constructed on the surface of cathodes.

The unique SEI and CEI layers, on the one hand, reduce the interfacial resistance and accelerate the lithium-ion transport. On the other hand, they effectively minimize the consumption of lithium salts and solvents, reduce the formation of by-products (Li_2S), and slow down the degradation rate of SEI/CEI. As a result, the Li||Ni83 cells exhibit 82.5 % capacity retention after 300 cycles at 1C (1C = 200 mA g^{-1}) with a 4.3 V cut-off voltage, and 85.5 % retention after 100 cycles at 1C with a 4.5 V cut-off voltage, far surpassing traditional carbonate ester-based electrolytes. More importantly, a pouch cell with an energy density of 450 Wh/kg is manufactured, and a reasonable cycling stability is demonstrated. This study demonstrates a simple, scalable, and cost-effective approach for developing ester-based electrolytes with $LiNO_3$ and FEC by regulating solvation structures to stabilize the CEI and SEI layers in high-voltage lithium metal batteries.

CRediT authorship contribution statement

Zhuijun Xu: Writing – original draft, Formal analysis, Data curation, Conceptualization. **Meilan Peng:** Writing – review & editing, Formal analysis, Data curation. **Guangjiu Pan:** Writing – review & editing, Formal analysis, Data curation. **Tianle Zheng:** Writing – review & editing, Formal analysis, Data curation. **Yiyao Xiao:** Writing – review & editing, Formal analysis, Data curation. **Weiping Xie:** Writing – review & editing, Formal analysis, Data curation. **Yinghui Li:** Writing – review & editing, Formal analysis, Data curation. **Jie Gao:** Writing – review & editing, Supervision, Resources. **Shanshan Yin:** Writing – review & editing, Visualization. **Qing Ji:** Writing – review & editing, Supervision, Resources. **Baohu Wu:** Writing – review & editing, Formal analysis, Data curation. **Yi Miao:** Writing – review & editing, Formal analysis, Data curation. **Siqi Shi:** Writing – review & editing, Formal analysis, Data curation. **Ya-Jun Cheng:** Writing – review & editing, Supervision, Resources, Project administration, Funding acquisition, Conceptualization. **Yonggao Xia:** Writing – review & editing, Supervision, Resources. **Peter Müller-Buschbaum:** Writing – review & editing, Supervision, Resources, Project administration, Funding acquisition, Conceptualization.

Declaration of competing interest

The authors declare that they have no known competing financial interests or personal relationships that could have appeared to influence the work reported in this paper.

Acknowledgement

P.M-B acknowledges funding from the Deutsche Forschungsgemeinschaft (DFG, German Research Foundation) via project MU1487/38–1 (AOBJ: 673749), by the International Research Training Group 2022 Alberta/Technical University of Munich International Graduate School for Environmentally Responsible Functional Hybrid Materials (ATUMS), and under Germany's Excellence Strategy EXC 2089/1 – 390776260 (e-conversion). This research is supported by the National Natural Science Foundation of China (52061135110), Natural Science Foundation of Zhejiang Province (Grant No LD22E020003), and the Ningbo Science & Technology Innovation 2025 Major Project (2021Z121, 2022Z021). G. Pan and T. Zheng acknowledge the financial support from the China Scholarship Council (CSC).

Supplementary materials

Supplementary material associated with this article can be found, in the online version, at doi:10.1016/j.ensm.2025.104779.

Data availability

Data will be available from https://doi.org/10.104459/2025mp1799287.

References

[1] Y. Liu, D. Lin, Y. Li, G. Chen, A. Pei, O. Nix, Y. Li, Y. Cui, Solubility-mediated sustained release enabling nitrate additive in carbonate electrolytes for stable lithium metal anode, Nat. Commun. 9 (1) (2018) 3656, https://doi.org/10.1038/s41467-018-06077-5.

[2] G. Brunklaus, P. Lennartz, M. Winter, Metal electrodes for next-generation rechargeable batteries, Nat. Rev. Electr. Eng. 1 (2024) 79, https://doi.org/10.1038/s44287-023-00006-5.

[3] T. Zheng, J. Xiong, X. Shi, B. Zhu, Y.-J. Cheng, H. Zhao, Y. Xia, Cocktail therapy towards high temperature/high voltage lithium metal battery via solvation sheath structure tuning, Energy Storag. Mater. 38 (2021) 599, https://doi.org/10.1016/j.ensm.2021.04.002.

[4] Y. Liang, W. Wu, D. Li, H. Wu, C. Gao, Z. Chen, L. Ci, J. Zhang, Highly stable lithium metal batteries by regulating the lithium nitrate chemistry with a modified eutectic electrolyte, Adv. Energy Mater. 12 (47) (2022) e2202493, https://doi.org/10.1002/aenm.202202493.

[5] Y.H. Tan, G.X. Lu, J.H. Zheng, F. Zhou, M. Chen, T. Ma, L.L. Lu, Y.H. Song, Y. Guan, J. Wang, Z. Liang, W.S. Xu, Y. Zhang, X. Tao, H.B. Yao, Lithium fluoride in electrolyte for stable and safe Lithium-metal batteries, Adv. Mater. 33 (42) (2021) e2102134, https://doi.org/10.1002/adma.202102134.

[6] X.R. Chen, Y.X. Yao, C. Yan, R. Zhang, X.B. Cheng, Q. Zhang, A diffusion–reaction competition mechanism to tailor lithium deposition for lithium-metal batteries, Angew. Chem. Int. Ed. 59 (20) (2020) 7743, https://doi.org/10.1002/anie.202000375.

[7] C. Yan, Y.X. Yao, X. Chen, X.B. Cheng, X.Q. Zhang, J.Q. Huang, Q. Zhang, Lithium nitrate solvation chemistry in carbonate electrolyte sustains high-voltage Lithium metal batteries, Angew. Chem. Int. Ed. 57 (43) (2018) 14055, https://doi.org/10.1002/anie.201807034.

[8] X.Q. Zhang, X. Chen, X.B. Cheng, B.Q. Li, X. Shen, C. Yan, J.Q. Huang, Q. Zhang, Highly stable lithium metal batteries enabled by regulating the solvation of lithium ions in nonaqueous electrolytes, Angew. Chem. Int. Ed. 57 (19) (2018) 5301, https://doi.org/10.1002/anie.201801513.

[9] W. Zhang, Y. Lu, L. Wan, P. Zhou, Y. Xia, S. Yan, X. Chen, H. Zhou, H. Dong, K. Liu, Engineering a passivating electric double layer for high performance lithium metal batteries, Nat. Commun. 13 (1) (2022) 2029, https://doi.org/10.1038/s41467-022-29761-z.

[10] Z. Piao, P. Xiao, R. Luo, J. Ma, R. Gao, C. Li, J. Tan, K. Yu, G. Zhou, H.M. Cheng, Constructing a stable interface layer by tailoring solvation chemistry in carbonate electrolytes for high-performance lithium-metal batteries, Adv. Mater. 34 (8) (2022) e2108400, https://doi.org/10.1002/adma.202108400.

[11] Y. Liu, Y. Tian, F. Kang, M. Wagemaker, B. Li, G. Chen, Stabilized P-F bond for sustainable and ultralong life high-energy lithium batteries, Adv. Funct. Mater. (2025) e19229, https://doi.org/10.1002/adfm.202519229.

[12] Y. Xia, P. Zhou, X. Kong, J. Tian, W. Zhang, S. Yan, W.-h. Hou, H.-Y. Zhou, H. Dong, X. Chen, P. Wang, Z. Xu, L. Wan, B. Wang, K. Liu, Designing an asymmetric ether-like lithium salt to enable fast-cycling high-energy lithium metal batteries, Nat. Energy 8 (9) (2023) 934, https://doi.org/10.1038/s41560-023-01282-z.
[13] L. Carbone, T. Coneglian, M. Gobet, S. Munoz, M. Devany, S. Greenbaum, J. Hassoun, A simple approach for making a viable, safe, and high-performances lithium-sulfur battery, J. Power Sources 377 (2018) 26, https://doi.org/10.1016/j.jpowsour.2017.11.079.
[14] K. Wang, W. Ni, L. Wang, L. Gan, J. Zhao, Z. Wan, W. Jiang, W. Ahmad, M. Tian, M. Ling, J. Chen, C. Liang, Lithium nitrate regulated carbonate electrolytes for practical Li-metal batteries: mechanisms, principles and strategies, J. Energy Chem. 77 (2023) 581, https://doi.org/10.1016/j.jechem.2022.11.017.
[15] Y. Wang, Z. Cao, Z. Ma, G. Liu, H. Cheng, Y. Zou, L. Cavallo, Q. Li, J. Ming, Weak solvent–Solvent interaction enables high stability of battery electrolyte, ACS Energy Lett 8 (3) (2023) 1477, https://doi.org/10.1021/acsenergylett.3c00052.
[16] X. Wang, S. Li, W. Zhang, D. Wang, Z. Shen, J. Zheng, H.L. Zhuang, Y. He, Y. Lu, Dual-salt-additive electrolyte enables high-voltage lithium metal full batteries capable of fast-charging ability, Nano Energy 89 (2021) 106353, https://doi.org/10.1016/j.nanoen.2021.106353.
[17] H. Yang, X. Chen, N. Yao, N. Piao, Z. Wang, K. He, H.-M. Cheng, F. Li, Dissolution–Precipitation dynamics in ester electrolyte for high-stability lithium metal batteries, ACS Energy Lett (2021) 1413, https://doi.org/10.1021/acsenergylett.1c00149.
[18] Q. Liu, Y. Xu, J. Wang, B. Zhao, Z. Li, H.B. Wu, Sustained-release nanocapsules enable long-lasting stabilization of Li anode for practical Li-metal batteries, Nano-micro Lett 12 (1) (2020) 176, https://doi.org/10.1007/s40820-020-00514-1.
[19] H. Yang, Q. Liu, Y. Wang, Z. Ma, P. Tang, X. Zhang, H.M. Cheng, Z. Sun, F. Li, An interlayer containing dissociated $LiNO_3$ with fast release speed for stable lithium metal batteries with 400 wh kg^{-1} energy density, Small 18 (25) (2022) e2202349, https://doi.org/10.1002/smll.202202349.
[20] N. Piao, S. Liu, B. Zhang, X. Ji, X. Fan, L. Wang, P.-F. Wang, T. Jin, S.-C. Liou, H. Yang, J. Jiang, K. Xu, M.A. Schroeder, X. He, C. Wang, Lithium metal batteries enabled by synergetic additives in commercial carbonate electrolytes, ACS Energy Lett. 6 (5) (2021) 1839, https://doi.org/10.1021/acsenergylett.1c00365.
[21] C. Liao, L. Han, W. Wang, W. Li, X. Mu, Y. Kan, J. Zhu, Z. Gui, X. He, L. Song, Y. Hu, Non-flammable electrolyte with lithium nitrate as the only lithium salt for boosting ultra-stable cycling and fire-safety lithium metal batteries, Adv. Funct. Mater. 33 (17) (2023) e2212605, https://doi.org/10.1002/adfm.202212605.
[22] L.P. Hou, N. Yao, J. Xie, P. Shi, S.Y. Sun, C.B. Jin, C.M. Chen, Q.B. Liu, B.Q. Li, X. Q. Zhang, Q. Zhang, Modification of nitrate ion enables stable solid electrolyte interphase in lithium metal batteries, Angew. Chem. Int. Ed. 61 (20) (2022) e202201406, https://doi.org/10.1002/anie.202201406.
[23] H. Chen, K. Chen, L. Luo, X. Liu, Z. Wang, A. Zhao, H. Li, X. Ai, Y. Fang, Y. Cao, $LiNO_3$ -based electrolytes via electron-donation modulation for sustainable nonaqueous lithium rechargeable batteries, Angew. Chem. Int. Ed. 63 (10) (2024) e202316966, https://doi.org/10.1002/anie.202316966.
[24] Y. Jie, X. Liu, Z. Lei, S. Wang, Y. Chen, F. Huang, R. Cao, G. Zhang, S. Jiao, Enabling high-voltage lithium metal batteries by manipulating solvation structure in ester electrolyte, Angew. Chem. Int. Ed. 59 (9) (2020) 3505, https://doi.org/10.1002/ange.201914250.
[25] Z. Wen, W. Fang, F. Wang, H. Kang, S. Zhao, S. Guo, G. Chen, Dual-salt electrolyte additive enables high moisture tolerance and favorable electric double layer for lithium metal battery, Angew. Chem. Int. Ed. 63 (13) (2024) e202314876, https://doi.org/10.1002/ange.202314876.
[26] Z. Jin, Y. Liu, H. Xu, T. Chen, C. Wang, Intrinsic solubilization of lithium nitrate in ester electrolyte by multivalent low-entropy-penalty design for stable lithium-metal batteries, Angew. Chem. Int. Ed. 63 (10) (2024) e202318197, https://doi.org/10.1002/ange.202314876.
[27] Q. Zhao, N.W. Utomo, A.L. Kocen, S. Jin, Y. Deng, V.X. Zhu, S. Moganty, G. W. Coates, L.A. Archer, Upgrading carbonate electrolytes for ultra-stable practical lithium metal batteries, Angew. Chem. Int. Ed. 61 (9) (2022) e202116214, https://doi.org/10.1002/anie.202116214.
[28] Q. Wang, C. Zhao, S. Wang, J. Wang, F. Wu, P. Ombrini, S. Ganapathy, S. Eustace, X. Bai, B. Li, M. Armand, D. Aurbach, M. Wagemaker, Interphase design for lithium-metal anodes, J. Am. Chem. Soc. 147 (11) (2025) 9365, https://doi.org/10.1021/jacs.4c15759.
[29] Q. Wang, C. Zhao, Z. Yao, J. Wang, F. Wu, S.G.H. Kumar, S. Ganapathy, S. Eustace, X. Bai, B. Li, J. Lu, M. Wagemaker, Entropy-driven liquid electrolytes for lithium batteries, Adv. Mater. 35 (17) (2023) e2210677, https://doi.org/10.1002/adma.202210677.
[30] N. Sun, R. Li, Y. Zhao, H. Zhang, J. Chen, J. Xu, Z. Li, X. Fan, X. Yao, Z. Peng, Anionic coordination manipulation of multilayer solvation structure electrolyte for high-rate and low-temperature lithium metal battery, Adv. Energy Mater. 12 (42) (2022) 2200621, https://doi.org/10.1002/aenm.202200621.
[31] L.N. Wu, J. Peng, Y.K. Sun, F.M. Han, Y.F. Wen, C.G. Shi, J.J. Fan, L. Huang, J.T. Li, S.G. Sun, High-energy density Li metal dual-ion battery with a lithium nitrate-modified carbonate-based electrolyte, ACS Appl. Mater. Interfaces. 11 (20) (2019) 18504, https://doi.org/10.1021/acsami.9b05053.
[32] Y. Xia, W. Hou, P. Zhou, Y. Ou, G. Cheng, C. Guo, F. Liu, W. Zhang, S. Yan, Y. Lu, Y. Zeng, K. Liu, Trace dual-salt electrolyte additive enabling a LiF-rich solid electrolyte interphase for high-performance lithium metal batteries, Nano Lett. 24 (2024) 12791, https://doi.org/10.1021/acs.nanolett.4c02983.
[33] X. Liu, L. Fang, X. Lyu, R.E. Winans, T. Li, Unveiling the liquid electrolyte solvation structure by small angle X-ray scattering, Chem. Mater. 35 (23) (2023) 9821, https://doi.org/10.1021/acs.chemmater.3c01648.
[34] X. Liu, S.-C. Lee, S. Seifer, R.E. Winans, L. Cheng, Y. Z, T. Li, Insight into the nanostructure of "water in salt" solutions: a SAXS/WAXS study on imide-based lithium salts aqueous solutions, Energy Storage Mater 45 (2022) 696, https://doi.org/10.1016/j.ensm.2021.12.016.
[35] Z. Peng, X. Cao, P. Gao, H. Jia, X. Ren, S. Roy, Z. Li, Y. Zhu, W. Xie, D. Liu, Q. Li, D. Wang, W. Xu, J.G. Zhang, High-power lithium metal batteries enabled by High-concentration acetonitrile-based electrolytes with vinylene carbonate additive, Adv. Funct. Mater. 30 (24) (2020) 2001285, https://doi.org/10.1002/adfm.202001285.
[36] Z. Lu, H. Yang, J. Sun, J. Okagaki, Y. Choe, E. Yoo, Conformational isomerism breaks the electrolyte solubility limit and stabilizes 4.9 V Ni-rich layered cathodes, Nat. Commun. 15 (1) (2024) 9108, https://doi.org/10.1038/s41467-024-53570-1.
[37] G. Yang, I.N. Ivanov, R.E. Ruther, R.L. Sacci, V. Subjakova, D.T. Hallinan, J. Nanda, Electrolyte solvation structure at solid-liquid interface probed by Nanogap surface-enhanced raman spectroscopy, ACS Nano 12 (10) (2018) 10159, https://doi.org/10.1021/acsnano.8b05038.
[38] S. Lei, Z. Zeng, H. Yan, M. Qin, M. Liu, Y. Wu, H. Zhang, S. Cheng, J. Xie, Nonpolar cosolvent driving LUMO energy evolution of methyl acetate electrolyte to afford lithium-ion batteries operating at - 60 °C, Adv. Funct. Mater. 33 (34) (2023) e2301028, https://doi.org/10.1002/adfm.202301028.
[39] J. Fu, X. Ji, J. Chen, L. Chen, X. Fan, D. Mu, C. Wang, Lithium nitrate regulated sulfone electrolytes for Lithium metal batteries, Angew. Chem. Int. Ed. 59 (49) (2020) 22194, https://doi.org/10.1002/ange.202009575.
[40] S. Zugmann, M. Fleischmann, M. Amereller, R.M. Gschwind, H.D. Wiemhöfer, H. J. Gores, Measurement of transference numbers for lithium ion electrolytes via four different methods, a comparative study, Electrochim. Acta 56 (11) (2011) 3926, https://doi.org/10.1016/j.electacta.2011.02.025.
[41] Y. Liu, X. Xu, M. Sadd, O.O. Kapitanova, V.A. Krivchenko, J. Ban, J. Wang, X. Jiao, Z. Song, J. Song, S. Xiong, A. Matic, Insight into the critical role of exchange current density on electrodeposition behavior of lithium metal, Adv. Sci. 8 (5) (2021) 2003301, https://doi.org/10.1002/advs.202003301.
[42] G.A. Giffin, The role of concentration in electrolyte solutions for non-aqueous lithium-based batteries, Nat. Commun. 13 (1) (2022) 5250, https://doi.org/10.1038/s41467-022-32794-z.
[43] W.G. Kidanu, L. Munkhaugen, C. Lian, P. Schweigart, J. Hamonnet, A.M. Svensson, On the moisture tolerance of LiFSI based lithium-ion batteries: a systematic study on NMC622/graphite full cells, Electrochim. Acta 508 (2024) 145213, https://doi.org/10.1016/j.electacta.2024.145213.
[44] S.S. Zhang, Unveiling the mystery of lithium bis(fluorosulfonyl)imide as a single salt in low-to-moderate concentration electrolytes of lithium metal and lithium-ion batteries, J. Electrochem. Soc. 169 (11) (2022) 110515, https://doi.org/10.1149/1945-7111/ac9f7d.
[45] K.M. Scheer, M. Tulloch, I. Hamam, J.J. Abraham, M.B. Johnson, M. Metzger, Anodic dissolution of the aluminum current collector in lithium-ion cells with LiFSI, $LiPF_6$, and $LiBF_4$, J. Electrochem. Soc. 172 (1) (2025) 010511, https://doi.org/10.1149/1945-7111/ada641.
[46] K. Kim, I. Park, S.-Y. Ha, Y. Kim, M.-H. Woo, M.-H. Jeong, W.C. Shin, M. Ue, S. Y. Hong, N.-S. Choi, Understanding the thermal instability of fluoroethylene carbonate in $LiPF_6$ -based electrolytes for lithium ion batteries, Electrochim. Acta 225 (2017) 358, https://doi.org/10.1016/S0378-7753(01)00746-7.
[47] T. Li, Z. Zhao, G. Zhao, B. Zhang, W. Huang, T. Wu, W. Jia, J. Luo, Y. Xu, Deciphering lithium deposition behavior in elemental alloy anodes for lithium metal batteries, Nano Lett 24 (2024) 15234, https://doi.org/10.1021/acs.nanolett.4c03387.
[48] Y. Chen, F. Huang, M. Xie, Y. Han, W. Li, Y. Jie, X. Zhu, T. Cheng, R. Cao, S. Jiao, Aluminum corrosion chemistry in high-voltage lithium metal batteries with LiFSI-based ether electrolytes, ACS Appl. Mater. Interfaces. 16 (36) (2024) 47581, https://doi.org/10.1021/acsami.4c09083.
[49] J. Peng, H. Zhang, Z. Zeng, H. Zhang, H. Pei, Q. Wu, Y. Shen, R. Guo, S. Cheng, J. Xie, Tailoring solvation structures via precise diluent engineering for high-rate 500 wh kg^{-1} lithium-metal batteries, Adv. Mater. (2025) e09109, https://doi.org/10.1002/adma.202509109.
[50] J.E. Morales-Ugarte, E. Bolimowska, H. Rouault, J. Santos-Peña, C.C. Santini, A. Benayad, EIS and XPS investigation on SEI layer formation during first discharge on graphite electrode with a Vinylene carbonate doped imidazolium based ionic liquid electrolyte, J. Phys. Chem. C 122 (32) (2018) 18223, https://doi.org/10.1021/acs.jpcc.8b03636.
[51] V. Winkler, T. Hanemann, M. Bruns, Comparative surface analysis study of the solid electrolyte interphase formation on graphite anodes in lithium-ion batteries depending on the electrolyte composition, Surf. Interface Anal. 49 (5) (2016) 361, https://doi.org/10.1002/sia.6139.
[52] D. Lu, X. Lei, S. Weng, R. Li, J. Li, L. Lv, H. Zhang, Y. Huang, J. Zhang, S. Zhang, L. Fan, X. Wang, L. Chen, G. Cui, D. Su, X. Fan, A self-purifying electrolyte enables high energy Li ion batteries, Energy Environ. Sci. 15 (8) (2022) 3331, https://doi.org/10.1039/d2ee00483f.
[53] T.S. Masashi Matsumoto, Naoki Takao, Masato Mogi, Tomoyuki Matsuda, Keisuke Ando, Daichi Imamura, Hideto Imai, Impact of FEC additive on SEI structure formed on a carbon negative electrode studied by HAXPES, ECS Trans 69 (2015) 13, https://doi.org/10.1149/MA2015-02/5/407.
[54] M.C.I. PALCHAN, H. ESTRADE-SZWARCKOPF, B. ROUSSEAU, Graphite fluorides: an xps study of a new type of C-F bonding, Chem. Phys. Lett. 157 (1989) 321, https://doi.org/10.1016/0009-2614(89)87255-0.
[55] O. Rosseler, M. Sleiman, V.N. Montesinos, A. Shavorskiy, V. Keller, N. Keller, M. I. Litter, H. Bluhm, M. Salmeron, H. Destaillats, Chemistry of NO_x on TiO_2 surfaces studied by ambient pressure XPS: products, effect of UV irradiation, water, and

coadsorbed K^+, J. Phys. Chem. Lett. 4 (3) (2013) 536, https://doi.org/10.1021/jz302119g.
[56] W. Yu, K.Y. Lin, D.T. Boyle, M.T. Tang, Y. Cui, Y. Chen, Z. Yu, R. Xu, Y. Lin, G. Feng, Z. Huang, L. Michalek, W. Li, S.J. Harris, J.C. Jiang, F. Abild-Pedersen, J. Qin, Y. Cui, Z. Bao, Electrochemical formation of bis(fluorosulfonyl)imide-derived solid-electrolyte interphase at Li-metal potential, Nat. Chem. 17 (2024) 246, https://doi.org/10.1038/s41557-024-01689-5.
[57] Y. Wang, T. Wang, D. Dong, J. Xie, Y. Guan, Y. Huang, J. Fan, Y.-C. Lu, Enabling high-energy-density aqueous batteries with hydrogen bond-anchored electrolytes, Matter 5 (1) (2022) 162, https://doi.org/10.1016/j.matt.2021.10.021.
[58] H.F. Bittner, Primary and secondary lithium passivation characteristics and effects in the Li/SO_2 couple, J. Electrochem. Soc. 136 (1989) 3147, https://doi.org/10.1149/1.2096418.
[59] Y. Jung, B. Kang, Understanding abnormal potential behaviors at the 1st charge in Li2S cathode material for rechargeable Li-S batteries, Phys. Chem. Chem. Phys. 18 (31) (2016) 21500, https://doi.org/10.1039/C6CP03146C.
[60] P. Shi, T. Li, R. Zhang, X. Shen, X.B. Cheng, R. Xu, J.Q. Huang, X.R. Chen, H. Liu, Q. Zhang, Lithiophilic LiC_6 layers on carbon hosts enabling stable Li metal anode in working batteries, Adv. Mater. 31 (8) (2019) e1807131, https://doi.org/10.1002/adma.201807131.
[61] B. Guo, P. Guo, G. Zhao, S. Liu, J. Shi, M. Huang, Z. Shi, H. Wang, Z. Yan, A solid–solution-based Li–Mg alloy for highly stable lithium metal anodes, Sustain. Energy Fuels 6 (18) (2022) 4137, https://doi.org/10.1039/D2SE00910B.
[62] D. Wang, H. Xu, W. Li, J. Zhang, Lithium-magnesium alloy as anode materials for Li-ion batteries: a first-principles calculation, J. Energy Storage 110 (2025) 115303, https://doi.org/10.1016/j.est.2025.115303.